



저작자표시-비영리-변경금지 2.0 대한민국

이용자는 아래의 조건을 따르는 경우에 한하여 자유롭게

- 이 저작물을 복제, 배포, 전송, 전시, 공연 및 방송할 수 있습니다.

다음과 같은 조건을 따라야 합니다:



저작자표시. 귀하는 원저작자를 표시하여야 합니다.



비영리. 귀하는 이 저작물을 영리 목적으로 이용할 수 없습니다.



변경금지. 귀하는 이 저작물을 개작, 변형 또는 가공할 수 없습니다.

- 귀하는, 이 저작물의 재이용이나 배포의 경우, 이 저작물에 적용된 이용허락조건을 명확하게 나타내어야 합니다.
- 저작권자로부터 별도의 허가를 받으면 이러한 조건들은 적용되지 않습니다.

저작권법에 따른 이용자의 권리는 위의 내용에 의하여 영향을 받지 않습니다.

이것은 [이용허락규약\(Legal Code\)](#)을 이해하기 쉽게 요약한 것입니다.

[Disclaimer](#)

Master of Science

**Synthesis and Photophysical Properties of TADF Compounds
with Planarized Boron–Carbonyl Hybrid Acceptors**

The Graduate School of the University of Ulsan

Department of Chemistry

Ina Nur Istiqomah

**Synthesis and Photophysical Properties of TADF Compounds
with Planarized Boron–Carbonyl Hybrid Acceptors**

Supervisor: Professor Min Hyung Lee

A Dissertation

Submitted to

The Graduate School of the University of Ulsan

In partial Fulfillment of the Requirements

For the Degree of

Master of Science

by

Ina Nur Istiqomah

Department of Chemistry

University of Ulsan, Korea

May 2022

Synthesis and Photophysical Properties of TADF Compounds with Planarized Boron–Carbonyl Hybrid Acceptors

This certifies that the dissertation of Ina Nur Istiqomah is approved.



Committee Chair Professor Sang Kook Woo



Committee Member Professor Jaehoon Jung



Committee Member Professor Min Hyung Lee

Department of Chemistry

University of Ulsan, Korea

May 2022

Synthesis and Photophysical Properties of TADF Compounds with Planarized Boron–Carbonyl Hybrid Acceptors

Abstract:

Thermally activated delayed fluorescence (TADF) with a fast reverse intersystem crossing (RISC) gives a great challenge to attain a high efficiency in OLED device performances. Since it has been demonstrated that strong spin orbit coupling (SOC) could facilitate a fast RISC, we designed and synthesized a series of boron-carbonyl hybrid compounds comprising 10*H*-phenoxazine as a fixed donors connected with different acceptors, boranthracenone (PXZBAO), boratetracenone (PXZBTO), and borapentacenone (PXZBPO). All compounds have small singlet-triplet energy splitting ($\Delta E_{ST} < 0.1$ eV), very short-lived delayed fluorescence lifetime ($\tau_d < 2$ μ s), and high k_{RISC} of ca. 10^6 s⁻¹, which supported the strong and efficient TADF properties. In particular, the compounds exhibited blue-shifted emission wavelength ($\lambda_{PL} = 619$ – 574 nm) and ($\lambda_{PL} = 609$ – 568 nm) in both toluene and host film respectively by the addition of the naphthyl group in the boron acceptors. This finding suggests that the $^3n\pi^*$ from boron-carbonyl units was gradually changed to $^3\pi\pi^*$ as the number of the naphthyl ring increased. Likewise, the role of $^3n\pi^*$ from boron-carbonyl unit lies on the T₂ level inducing strong SOC with the 1CT (S₁) state so that the fast RISC could be accelerated. The details of synthesis, characterization, photophysical properties and theoretical studies will be discussed.

Table Of Contents

Abstract.....	iv
Table of Contents.....	v
List of Figures.....	vii
List of Tables.....	ix
I. INTRODUCTION.....	1
1. Organic Light Emitting Diodes (OLED).....	1
2. Thermally Activated Delayed Fluorescence (TADF).....	2
3. Boron-based Donor (D)–Acceptor (A) TADF Emitter.....	4
4. Research Scope.....	7
II. EXPERIMENT.....	8
1. Chemical and Instrumentation.....	8
2. Synthesis.....	8
2.1. 5,5-Dimethyl-5,12-dihydrobenzo[b]naphtho[2,3-e]siline (2c).....	8
2.2. 5-(4-Bromo-2,6-di(prop-1-en-2-yl)phenyl)-5,12-dihydrobenzo[b]naphtho[2,3-e]borinine (2d).....	9
2.3. 2-Bromo-4,4,14,14-tetramethyl-8,14-dihydro-4H-3a2-boraphenaleno[2,1,9,8-defg]tetracene (2e).....	9
2.4. 2-Bromo-4,4,14,14-tetramethyl-4H-3a2-boraphenaleno[2,1,9,8-defg]tetracene-8(14H)-one (2f).....	10
2.5. 6,6-Dimethyl-6,13-dihydrodinaphtho[2,3-b:2',3'-e]siline (3c).....	10
2.6. 6-(4-Bromo-2,6-di(prop-1-en-2-yl)phenyl)-6,13-dihydrodinaphtho[2,3-b:2',3'-e]borinine (3d).....	11
2.7. 2-Bromo-4,4,16,16-tetramethyl-10,16-dihydro-4H-3a2-boraphenaleno[2,1,9,8-fghi]pentacene (3e).....	11
2.8. 2-Bromo-4,4,16,16-tetramethyl-4H-3a2-boraphenaleno[2,1,9,8-fghi]pentacene-10(16H)-one (3f).....	11

2.9.	Synthesis of PXZBAO (1)	12
2.10.	Synthesis of PXZBTO (2).....	12
2.11.	Synthesis of PXZBPO (3).....	13
3.	X-ray Crystallography	13
4.	Photophysical Measurements.....	13
5.	Cyclic Voltammetry.....	14
III.	RESULT AND DISCUSSION	15
1.	Synthesis and Characterization	15
2.	Photophysical Properties.....	30
3.	Electrochemical Properties	37
4.	Theoretical Calculation.....	38
5.	Electroluminescent Properties	40
IV.	CONCLUSION.....	42
V.	REFERENCES	43

List of Figures

Figure 1. Schematic Overview of OLEDs Device.....	2
Figure 2. Working Principle of OLEDs	2
Figure 3. The Generation of OLEDs.....	3
Figure 4. Characteristic features of boron atom in the π -conjugated materials.	4
Figure 5. π -conjugation with Boron.....	5
Figure 6. Molecular Structure of (a) BuCzMeOB; (b) TDBA-DI; (c) PzTDBA; (d) PzDBA; (e) TMCzBCO; (f) DMACBCO.....	6
Figure 7. ^{13}C (top) and ^1H (bottom) NMR spectra of 2c in CDCl_3 (* from water and † from residual CHCl_3).	18
Figure 8. ^{11}B (top), ^{13}C (middle), and ^1H (bottom) NMR spectra of 2d (* from water and † from residual CHDCl_2).....	19
Figure 9. ^{11}B (top), ^{13}C (middle), and ^1H (bottom) NMR spectra of 2e (* from water and † from residual CHDCl_2).....	20
Figure 10. ^{11}B (top), ^{13}C (middle), and ^1H (bottom) NMR spectra of 2f (* from water and † from residual CHDCl_2).....	21
Figure 11. ^{13}C (top) and ^1H (bottom) NMR spectra of 3c (* from water and † from residual CHCl_3).	22
Figure 12. ^{11}B (top), ^{13}C (middle), and ^1H (bottom) NMR spectra of 3d in CD_2Cl_2 (* from water and † from residual CHDCl_2).	23
Figure 13. ^1H NMR spectra of 3e in CD_2Cl_2 (* from water and † from residual CHDCl_2). ...	24
Figure 14. ^1H NMR spectra of 3f in CD_2Cl_2 (* from water and † from residual CHDCl_2).	24
Figure 15. ^{11}B (top), ^{13}C (middle), and ^1H (bottom) NMR spectra of PXZBAO (1) (* from water and † from residual CHDCl_2).	25
Figure 16. ^{11}B (top), ^{13}C (middle), and ^1H (bottom) NMR spectra of PXZBTO (2) (* from water and † from residual CHDCl_2).	26

Figure 17. ^{11}B (top), ^{13}C (middle), and ^1H (bottom) NMR spectra of PXZBPO (3) (\dagger from residual CH_2Cl_2).	27
Figure 18. X-ray crystal structure of PXZBPO (3) (50% thermal ellipsoids). H atoms are omitted for clarity. Color code: blue = nitrogen; brown = boron; red = oxygen.....	28
Figure 19. TGA Curves of PXZBAO (1), PXZBTO (2), and PXZBPO (3).....	30
Figure 20. UV/vis absorption (left) and PL spectra (right) of PXZBAO (1), PXZBTO (2), and PXZBPO (3) in toluene (2.0×10^{-5} M) at 298 K.	31
Figure 21. PL spectra of PXZBAO (1), PXZBTO (2), and PXZBPO (3) in 5 wt% mCBP at 298 K.	32
Figure 22. Transient PL decay curves of PXZBAO (left), PXZBTO (middle), PXZBPO (right) in oxygen-free toluene at 298 K.	34
Figure 23. The temperature dependant of the transient PL decay from 80 to 295 K (PXZBPO).	34
Figure 24. Fluorescence and phosphorescence spectra of PXZBAO (top), PXZBTO (middle), and PXZBPO (bottom) in toluene at 77 K.	35
Figure 25. NICS (Nucleus-Independent Chemical Shift) value of PXZBAO (1), PXZBTO (2), PXZBPO (3).	36
Figure 26. Cyclic voltammograms of PXZBAO (1), PXZBTO (2), and PXZBPO (3).....	37
Figure 27. Frontier MOs (HOMO and LUMO) of PXZBAO (1), PXZBTO (2), PXZBPO (3) at their ground state (S_0) geometries.	39
Figure 28. Natural transition orbitals (NTOs) of compounds PXZBAO (1), PXZBTO (2), and PXZBPO (3) for the transitions from the S_0 state to the S_1 , T_1 , and T_2 states.	39
Figure 29. (a) Device Structure of the proposed TADF-OLEDs. (b) Current density-voltage-luminance (J - V - L) characteristics of D1–D3. (c) The EL spectra of D1–D3. (d) The EQE–luminance of D1–D3 in the linear scale.	40

List of Tables

Table 1. Selected bond lengths (\AA) and angles ($^{\circ}$) of PXZBPO.....	28
Table 2. Crystallographic data and parameters for PXZBPO.....	29
Table 3. Photophysical properties of PXZBAO, PXZBTO, and PXZBPO.....	33
Table 4. Photophysical data of PXZBAO, PXZBTO, and PXZBPO at 77 K.	36
Table 5. Cyclic Voltammetry Data of PXZBAO, PXZBTO, and PXZBPO.	37

I. INTRODUCTION

1. Organic Light Emitting Diodes (OLED)

An organic light emitting diode (OLED), also known as organic electroluminescent diode, is a type of light emitting diode (LED) which the emissive electroluminescent layer is composed of a layer of organic materials, typically aromatic small molecules. OLED displays are now routinely found in digital displays in devices such as smartphones and high-end televisions due to their lower power consumption, high brightness, color purity, light weight, large viewing angle and flexible, compared to traditional LCD displays¹. Back to the first experiments to generate light from organic materials was discovered in 1963 by W. Helfrich *et al.*, through the observation in anthracene single crystal,² followed by the first practical OLED was built by Tang and VanSlyke in 1987 by reporting a double-layered device using tris (8-hydroxyquinoline) aluminum (Alq₃) as the emitting and electron-transporting layer. This report demonstrated a green-emitting device, and the driving-voltage was lowered below 10 V and the efficiency was increased up to 1.51 m/W.³ Since the pioneering of this technology, many studies in organic electronics field were developed enormously for the following years.

OLED devices typically consist of a thin layer of a host material which is doped with an organic emitter material situated between the cathode and anode. During the operation, the charge carriers, that is, electrons and holes, are obtained at the cathode and anode, respectively, by applying an electric voltage. Then, the charge carriers are injected into the electron and hole injection layers. Afterwards, the electrons and holes flow through the electron and hole transport layers into the emissive layer (EML), where the recombination of the charge carriers and the formation of excitons takes place. The recombination of the electrons and holes (excitons) relax radiatively from the excited state to the ground state by emitting the light.⁴

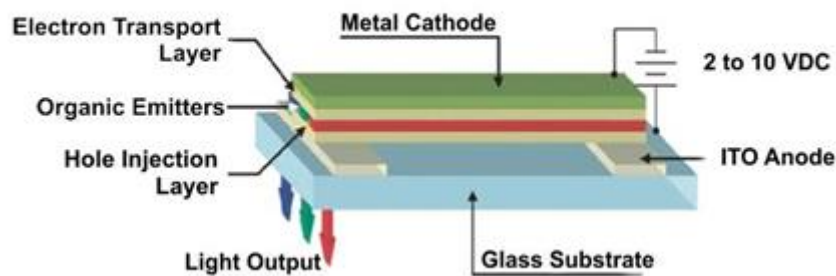


Figure 1. Schematic Overview of OLEDs Device

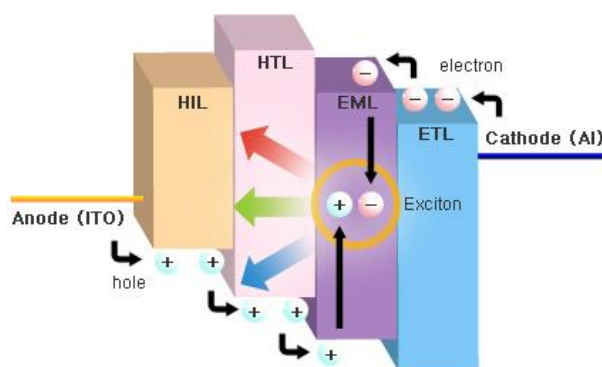


Figure 2. Working Principle of OLEDs

2. Thermally Activated Delayed Fluorescence (TADF)

The first generation of OLEDs are known as fluorescent OLEDs exhibited lower efficiency due to usage of only 25% of singlet excitons formed during the exciton recombination process.⁵ To increase the remaining 75% of excitons in triplet states, phosphorescent material was developed as emitters for the second generation of OLEDs. The heavy metal atoms such as iridium or platinum, was applied to the emitters through an enhanced spin-orbit coupling, resulting complexes which accelerate the radiative deactivation through phosphorescence from the lowest-lying triplet state T_1 to the ground state S_0 and facilitate ISC from the lowest-lying singlet state S_1 to T_1 .⁶

An alternative way of harvesting 75% of triplet excitons without incorporating a heavy metal is called as thermally activated delayed fluorescence (TADF). The typical of the ideal TADF process by electroluminescence (EL), 25% light emission is from prompt fluorescence, and 75% of light emission is from delayed fluorescence by reverse intersystem crossing. The prompt fluorescence is caused by fast $S_1 \rightarrow S_0$ transition with an excited state lifetime (τ) of

several nanoseconds, while the delayed fluorescence is brought by slow $T_1 \rightarrow S_1 \rightarrow S_0$ transition with a (τ) longer than microseconds, where T_1 is the triplet excited state, S_1 is the singlet excited state, and S_0 is the singlet ground state. The detailed of three generations of OLEDs were described in (Figure 3). In the PL process, only singlet excitons are generated by photoexcitation and the singlet excitons are converted into triplet excitons by an intersystem crossing (ISC) process. The triplet excitons are either converted into singlet excitons again by a reverse intersystem crossing (RISC) process or wasted by an internal conversion process. The upconverted triplet excitons decay radiatively by singlet emission or nonradiatively by internal conversion.⁷

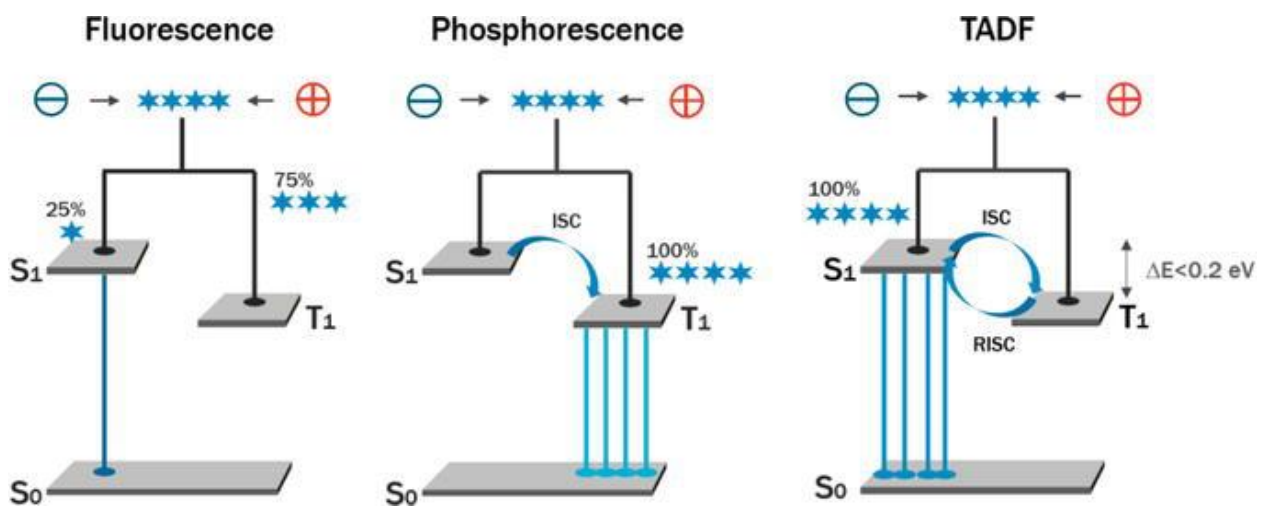


Figure 3. The Generation of OLEDs

For efficient TADF emission, there are several requirements that need to be satisfied such as assuring a small splitting energy between singlet and triplet excited states (ΔE_{ST}), while keep maintaining a high photoluminescence quantum yield (PLQY). ΔE_{ST} is the most important physical parameter of TADF emitters, which is related with the rate of reverse intersystem crossing (k_{RISC}) by the following equation:

$$k_{RISC} \propto \exp\left(-\frac{\Delta E_{ST}}{k_B T}\right)$$

Small ΔE_{ST} could increase the k_{RISC} and triplet-to-singlet conversion efficiency, which may increase the EQE of TADF emitters. Therefore, most TADF emitters were designed to have small ΔE_{ST} for high EQE in TADF devices. Generally, ΔE_{ST} depends on the exchange energy

gap between singlet excited state and triplet excited state. The triplet state is stabilized by the presence of unpaired electrons in different orbitals, while the singlet state is relatively destabilized by the presence of paired electrons in the same orbital. ΔE_{ST} can be reduced by decreasing the HOMO and LUMO overlap, which can be accomplished by spatially separating HOMO and LUMO through donor-acceptor structures or conjugation-breaking molecular structure. In most cases, donor-acceptor structures are employed to obtain the small ΔE_{ST} in the TADF emitters.⁷

3. Boron-based Donor (D)–Acceptor (A) TADF Emitter

Boron-based TADF materials have received enormous attract in the last few years as a potentially candidates in the optoelectronic devices due to their excellent photophysical and electrochemical properties. Boron atom has a vacant p-orbital which gives an electron deficient nature or Lewis acidic nature that could raise its electron accepting ability (**Figure 4**). This electron deficient boron can make a π -conjugation with organic-conjugated system through empty p_z orbital of boron and π -orbital of carbon (**Figure 5**).⁸ High Lewis acidic triarylboron compound in D-A organic π -conjugated system function could act as a good acceptor through $p\pi-\pi^*$ conjugation. When it was incorporated with the suitable electron donors such as amines acridan, phenoxazine and phenothiazine could possess a large electronic dipole, which promote donor-acceptor strong intramolecular charge-transfer (ICT) upon excitation with light.⁹

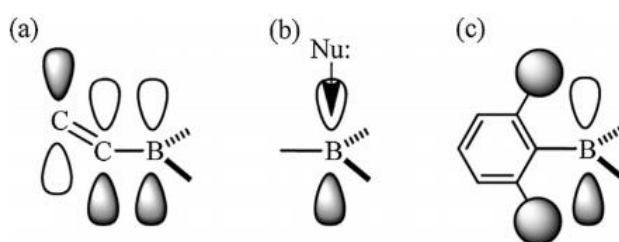


Figure 4. Characteristic features of boron atom in the π -conjugated materials.

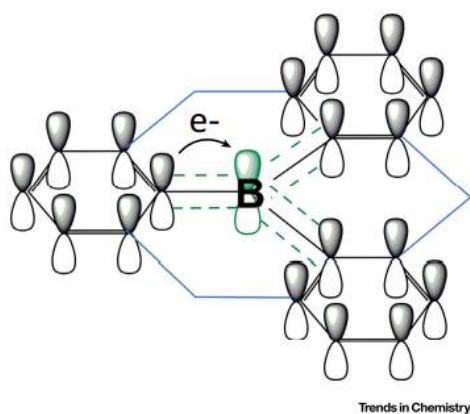


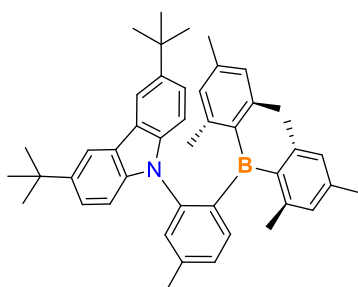
Figure 5. π -conjugation with Boron

Recently, many TADF materials with boron acceptors have been reported with good performances. In 2018, our group prepared a series of *ortho*-carbazole-appended triarylboron compounds substituted with various substituents. The retention of a twisted donor(D)-acceptor (A) structure enabled by *ortho* D-A connectivity and bulky triarylboron leads to small energy splitting between singlet and triplet excited states. The blue OLEDs incorporating a BuCzMeoB emitter exhibit a very high EQE of 32.8% at CIE (0.135, 0.266).¹⁰ Kwon et. al designed symmetric and rigid oxygen-bridged boron acceptors and diindolocarbazole as a donor (TDBA-DI). This emitter gives a high PLQY of 99% in DBFPO host. The device performances showed an extremely high EQE of 38.15% in the blue region with low roll-off characteristics of 25.2% at high luminance up to 5,000 cd m⁻².¹¹ Further in 2021, the same group designed a series of acceptor-donor-acceptor type red TADF emitters by applying a rigid oxygen bridged boron acceptor and dihydrophenazine donor moieties. These compounds showed small ΔE_{ST} of 0.06, 0.05 eV for PzTDBA and PzDBA, which could accelerate the fast RISC process. These materials also revealed a high PLQY of over 85%. Further, the fabricated OLEDs with PzTDBA and PzDBA as an emitting dopant showed a maximum EQE of 30.3% and 21.8% at 588 nm and 613 nm EL emission, respectively.¹²

Most recently, our group introduced two D-A-type TADF emitters (TMCzBCO and DMACBCO) employing a boron-carbonyl (BCO) as a hybrid acceptor unit. The emitters possess a $^3n\pi^*$ state of the BCO unit as an intermediate local triplet excited state (2LE , T_2) inducing to the large spin-orbit coupling between the T_2 and excited singlet (S_1) states. Accordingly, a fast RISC with rate constants (k_{RISC}) exceeding 10^6 s⁻¹ was accomplished, as well as short exciton lifetimes (~ 1 μ s) were realized. The device performance of TMCzBCO and DMACBCO achieved a high maximum EQEs of 24.7% in the green emission and 28.4%

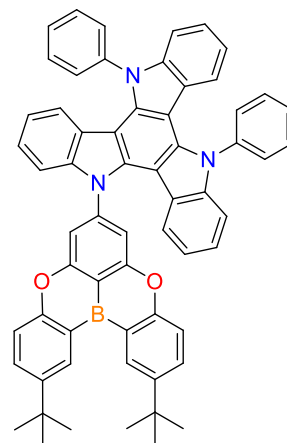
in the yellow emission and the low efficiency roll-off, with EQEs exceeding 20% at 5,000 cd/m^2 and 18% at 10,000 cd/m^2 .¹¹ This finding is important since the details of the impact of $^3n\pi^*$ system for the enhancement of the RISC rate still rarely been discussed.¹³

a)



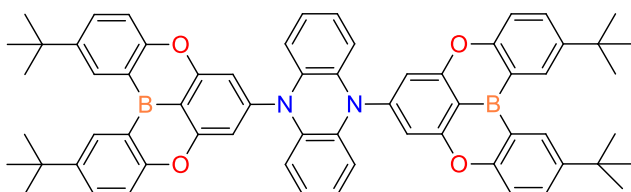
Lee, Y. H. et al. *Adv. Opt. Mater.*
2018, 1800385.

b)



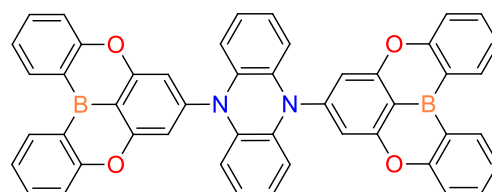
Ahn, D. H. et al. *Nat. Photonics.*
2019, 13, 540

c)

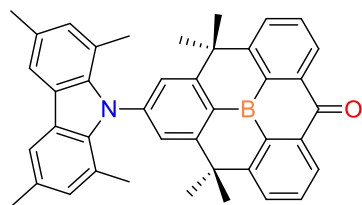


Karthik, D. et al. *Adv. Mater.*
2021, 33, 2007724

d)



e)



Lee, Y. H. et al. *Chem. Eng. J.*
2021, 423, 13022.

f)

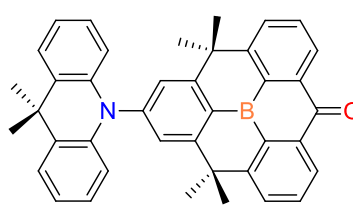


Figure 6. Molecular Structure of (a) BuCzMeOB; (b) TDBA-DI; (c) PzTDBA; (d) PzDBA; (e) TMCzBCO; (f) DMACBCO

4. Research Scope

To achieve an efficient TADF, the exciton up-conversion from triplet-to-singlet by reverse intersystem crossing (RISC) is important to realize 100% internal quantum efficiencies (IQEs) under electrical excitation. Hence, TADF emitters with a small energy splitting (ΔE_{ST}) between the excited singlet (S_1) and triplet (T_1) states is desirable to accelerate the rate of RISC. Small ΔE_{ST} can be achieved by separating the HOMO and LUMO typically based on the donor (D)-acceptor (A)-type molecular designs. Nevertheless, the charge transfer (CT) character between S_1 and T_1 was inevitably give a small spin orbit coupling (SOC) leading to inefficient RISC, thereby, long-lived delayed fluorescence is provided.^{14,15} Recently, the RISC rate can be increased by the strong SOC between the 1CT state and 3LE state as a T_2 state through vibronic coupling between 3CT (T_1) and 3LE (T_2) states.¹⁶⁻¹⁹ Hence, the proper choice of a 3LE state as an intermediate state play an important role to enhance the SOC matrix elements in TADF emitter. Boron-carbonyl acceptor (BCO) was previously reported to provide the $^3n\pi^*$ as a 3LE (T_2) state in D-A type emitters giving the effective SOC with the 1CT state.¹³ In this study, the BCO acceptor was modified by increasing the number of the naphthyl group to control the T_2 state and to investigate the emission control and photophysical properties of the compounds. Three TADF compounds, where phenoxazine as a donor connected with different acceptors, boraanthracenone (PXZBAO), boratetracenone (PXZBTO), and borapentacenone (PXZBPO) were designed and prepared in several steps. All compounds were analyzed by NMR spectroscopy, PXZBPO structure were analyzed by single crystals suitable for X-ray crystallography obtained by slow evaporation of a solution. Photophysical properties including UV-Vis absorption, emission spectra, and emission lifetimes were measured in toluene solution and host film. In addition, theoretical study was performed to investigate the geometric and electronic properties in their ground state and excited state. As a result, we observed that the $^3n\pi^*$ from boron-carbonyl unit in T_2 state was gradually changed to $^3\pi\pi^*$, and the emission wavelength was blue-shifted along with the increase of the number of the naphthyl ring in the boron acceptors.

II. EXPERIMENT

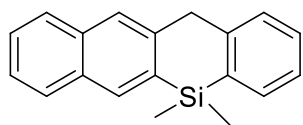
1. Chemical and Instrumentation

All operations were performed under an inert nitrogen atmosphere using standard Schlenk and glovebox techniques. Anhydrous-grade solvents (Aldrich) were dried over activated molecular sieves (5Å). Spectrophotometric-grade toluene was used as received from Merck. Commercial reagents were used without further purification after purchase. Deuterated solvents from Eurisotop were used. NMR spectra were recorded on a Bruker AM 300 (300.13 MHz for ^1H , 75.47 MHz for ^{13}C) or a Bruker AVANCE III HD 400 (128.38 MHz for ^{11}B) spectrometer at ambient temperature. Chemical shifts are given in ppm, and are referenced against external Me_4Si (^1H , ^{13}C) and $\text{BF}_3 \cdot \text{OEt}_2$ (^{11}B). Mass spectra were obtained using a JEOL JMS700 high-resolution EI-mass spectrometer (HR EI-MS) at the Korea Basic Science Institute, Daegu, Korea. Elemental analyses were performed on a Flash 2000 elemental analyzer (Thermo Scientific). Melting (mp) points were measured by Melting Point Apparatus SMP30 (Stuart Equipment). Thermogravimetric analysis (TGA) was performed with a TA Instruments Q50 under an N_2 atmosphere at a heating rate of 20 $^\circ\text{C}/\text{min}$. Cyclic voltammetry experiments were carried out using a CHI600E system

2. Synthesis

The compounds were prepared according to **Scheme 1**. 2-Bromo-4,4,12,12-tetramethyl-4,12-dihydro-8*H*-3a2-boradibenzo[cd,mn]pyren-8-one (Br-BCO) were prepared from the reported procedure.²⁰ Full experimental details are given below.

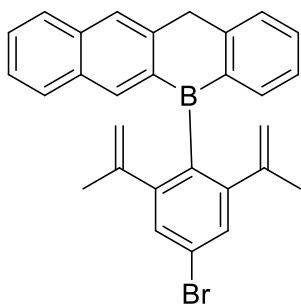
2.1. 5,5-Dimethyl-5,12-dihydrobenzo[*b*]naphtho[2,3-*e*]siline (2c)



To a solution of 2-bromo-3-(2-bromobenzyl)naphthalene (**2b**) (3.3 g, 8.89 mmol) in THF (20 mL) cooled at -78°C was added *n*-BuLi (2.5 M in hexane, 7.1 mL, 17.8 mmol) dropwise. After the completion of the addition, the reaction mixture was stirred at this temperature for 2 h. To the reaction mixture was then added dichlorodimethylsilane (1.07 mL, 1.15 g, 8.89 mmol). The reaction mixture was allowed to warm to room temperature and was stirred overnight. After the addition of a saturated aqueous NH_4Cl solution (20 mL), the organic layer was separated, and the aqueous layer was extracted with ether (10 mL) three times. The combined organic layer was dried over MgSO_4 , filtered, and evaporated under reduced pressure. The crude product was purified by silica gel column chromatography (dichloromethane/hexane = 1:4, v/v) to give 2.1 g (7.65 mmol, 86%) of **2c** as a yellow oil. ^1H NMR (CDCl_3): δ 8.09 (s, 1H), 7.86–7.77 (m, 3H), 7.65–7.61 (m, 1H), 7.46 (ddd, $J = 7.0, 5.6, 3.4$ Hz, 2H), 7.40–7.27 (m, 3H), 4.26 (s, 2H), 0.57 (s,

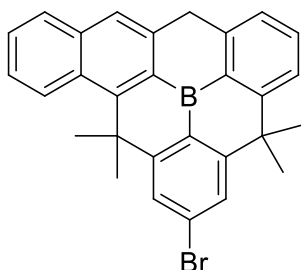
6H). ^{13}C NMR (CDCl_3): δ 142.1, 134.8, 133.9, 133.8, 133.0, 131.7, 129.3, 129.0, 128.5, 127.9, 127.7, 127.4, 126.5, 125.8, 125.4, 125.3, 41.9, -3.0 .

2.2. 5-(4-Bromo-2,6-di(prop-1-en-2-yl)phenyl)-5,12-dihydrobenzo[*b*]naphtho[2,3-*e*]borinine (**2d**)



To a solution of **2c** (2.1 g, 7.65 mmol) was added an excess BBr_3 at 50°C and the mixture was stirred for 14 h. Excess BBr_3 was removed under reduced pressure to give a red solid. The lithium salt of 2-bromo-1,3-bis(prop-1-en-2-yl)benzene (1.48 g, 4.08 mmol) in toluene (15 mL), which was simultaneously prepared with *n*-BuLi (2.5 M in hexane, 1.63 mL, 4.08 mmol) in a second Schlenk flask, was cooled at 0°C , and the solution was slowly transferred to the red solid by cannula at 0°C . The reaction mixture was stirred at room temperature overnight. After the addition of a saturated aqueous NH_4Cl solution (20 mL), the organic layer was separated, and the aqueous layer was extracted with ether (10 mL) three times. The combined organic layer was dried over MgSO_4 , filtered, and evaporated under reduced pressure. The crude product was purified by silica gel column chromatography (dichloromethane/hexane = 1:5, v/v) to give 2.2 g (4.74 mmol, 62%) of **2d** as a pink powder. ^1H NMR (CD_2Cl_2): δ 8.20 (s, 1H), 7.93 (s, 1H), 7.84 (t, $J = 8.7$ Hz, 2H), 7.62 (d, $J = 7.4$ Hz, 1H), 7.55–7.50 (m, 5H), 7.42 (t, $J = 7.5$ Hz, 1H), 7.30–7.24 (m, 1H), 4.66–4.62 (m, 2H), 4.57 (d, $J = 6.0$ Hz, 4H), 1.89 (s, 6H). ^{13}C NMR (CD_2Cl_2): δ 148.8, 146.8, 146.6, 141.4, 138.7, 136.9, 135.4, 132.1, 131.6, 129.0, 128.2, 128.0, 127.7, 127.0, 125.5, 125.5, 125.2, 121.4, 117.4, 38.0, 23.8. ^{11}B NMR (CD_2Cl_2): δ 48.4.

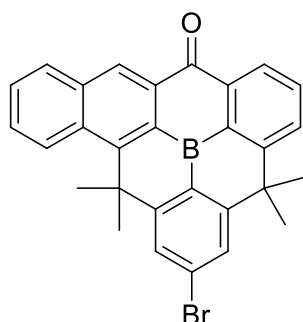
2.3. 2-Bromo-4,4,14,14-tetramethyl-8,14-dihydro-4H-3a2-boraphenaleno[2,1,9,8-defg]tetracene (**2e**)



In a 500 mL Schlenk flask containing **2d** (600 mg, 1.29 mmol) and 2 equiv of $\text{Sc}(\text{OTf})_3$ (1.27 g, 2.58 mmol) was added 1,2-dichloroethane (DCE, 210 mL). The reaction mixture was refluxed for 3 d. After the addition of distilled water (50 mL), the organic layer was separated, and the aqueous layer was extracted with dichloromethane (20 mL) three times. The combined organic layer was dried over MgSO_4 , filtered, and evaporated under reduced pressure. The crude product was purified by silica gel column chromatography (dichloromethane/hexane = 1:4, v/v), and then recrystallized with dichloromethane/methanol to give 348 mg (0.75 mmol, 58%) of **2e** as a yellow powder. ^1H

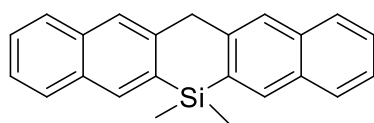
NMR (CD₂Cl₂): δ 8.70 (dd, J = 6.5, 3.7 Hz, 1H), 7.94 (dd, J = 11.0, 3.9 Hz, 3H), 7.85 (d, J = 1.5 Hz, 1H), 7.72–7.66 (m, 2H), 7.59 (dd, J = 6.5, 3.3 Hz, 2H), 7.46 (d, J = 3.0 Hz, 1H), 4.75 (s, 2H), 2.16 (s, 6H), 1.79 (s, 6H). ¹³C NMR (CD₂Cl₂): δ 163.3, 157.7, 156.1, 153.6, 145.9, 140.6, 137.6, 132.9, 129.8, 128.8, 128.4, 128.3, 128.0, 127.2, 126.4, 126.3, 125.0, 124.1, 124.1, 44.0, 42.6, 37.5, 34.2, 32.9. ¹¹B NMR (CD₂Cl₂): δ 46.7.

2.4. 2-Bromo-4,4,14,14-tetramethyl-4H-3a2-boraphenaleno[2,1,9,8-defg]tetracene-8(14H)-one (2f)



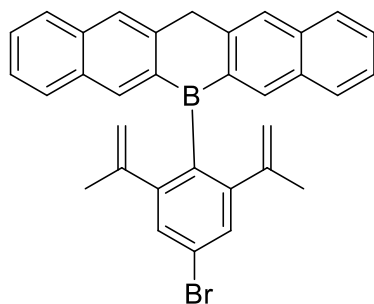
To a solution of **2e** (348 mg, 0.75 mmol) in dichloromethane (10 mL), pyridinium chlorochromate complex (PCC) (421 mg, 1.95 mmol) was added and the reaction mixture was stirred at 50 °C overnight. The reaction mixture was diluted with dichloromethane, passed through a pad of Celite, and concentrated *in vacuo*. The crude product was purified by flash chromatography (hexane/ethyl acetate = 1:3, v/v), and then recrystallized with a solution of dichloromethane/methanol to give 247 mg (0.52 mmol, 69%) of **2f** a yellow powder. ¹H NMR (CD₂Cl₂): δ 8.89 (s, 1H), 8.74 (d, J = 8.8 Hz, 1H), 8.32 (d, J = 7.6 Hz, 1H), 8.21 (d, J = 8.1 Hz, 1H), 8.01 (dd, J = 16.3, 4.7 Hz, 2H), 7.87 (dd, J = 14.8, 7.1 Hz, 2H), 7.81–7.74 (m, 1H), 7.73–7.65 (m, 1H), 2.16 (s, 6H), 1.82 (s, 6H). ¹³C NMR (CD₂Cl₂): δ 188.7, 163.5, 157.5, 155.8, 154.0, 138.5, 137.5, 133.7, 132.8, 132.5, 131.7, 130.0, 129.4, 128.7, 128.3, 127.6, 127.5, 127.3, 125.5, 44.3, 42.8, 33.4, 32.2. ¹¹B NMR (CD₂Cl₂): δ 45.6. HRMS (EI): m/z [M]⁺ calcd for C₂₉H₂₂BBrO: 476.0952; found: 476.0945.

2.5. 6,6-Dimethyl-6,13-dihydrodinaphtho[2,3-b:2',3'-e]siline (3c)



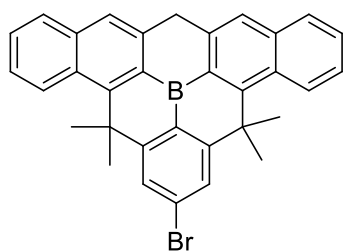
To a solution of bis(3-bromonaphthalen-2-yl)methane (**3b**) (1.67 g, 3.9 mmol) in ether (25 mL) cooled at 0 °C was added *n*-BuLi (2.5 M in hexane, 3.1 mL, 7.8 mmol) dropwise. After stirring for 2 h, dichlorodimethylsilane (0.47 mL, 0.5 g, 3.9 mmol) was slowly added to the reaction mixture at 0 °C. The reaction mixture was stirred at room temperature for 12 h. Work-up and purification of the crude product by silica gel column chromatography (dichloromethane/hexane = 1/4, v/v) afforded 898 mg (2.76 mmol, 70%) of **3c** as a white powder. ¹H NMR (CDCl₃): δ 8.11 (s, 1H), 7.89–7.76 (m, 3H), 7.46 (tt, J = 6.7, 5.3 Hz, 2H), 4.40 (s, 1H), 0.66 (s, 3H). ¹³C NMR (CDCl₃): δ 142.3, 135.0, 134.2, 133.9, 131.9, 127.9, 127.5, 126.6, 125.6, 125.5, 42.4, –2.7.

2.6. 6-(4-Bromo-2,6-di(prop-1-en-2-yl)phenyl)-6,13-dihydrodinaphtho[2,3-b:2',3'-e]borinine (3d)



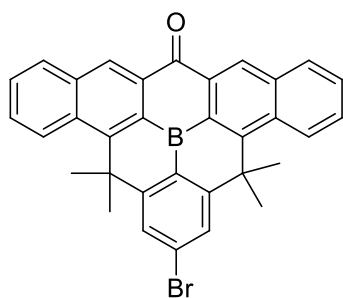
This compound was prepared in a manner analogous to the synthesis of **2d** using **3c** (508 mg, 1.4 mmol) to give a yellow powder of **3d** (402 mg, 0.784 mmol, yield = 56%). ¹H NMR (CD₂Cl₂): δ 8.23 (s, 1H), 7.95 (s, 1H), 7.85 (t, *J* = 8.9 Hz, 2H), 7.60–7.51 (m, 2H), 7.43 (ddd, *J* = 8.0, 6.8, 1.2 Hz, 1H), 4.71 (s, 1H), 4.66 (s, 2H), 1.89 (s, 3H). ¹³C NMR (CD₂Cl₂): δ 149.0, 147.1, 141.6, 139.0, 135.6, 131.6, 129.1, 128.4, 127.9, 127.1, 125.3, 125.2, 121.5, 117.5, 38.2, 23.9. ¹¹B NMR (CD₂Cl₂): δ 45.5.

2.7. 2-Bromo-4,4,16,16-tetramethyl-10,16-dihydro-4H-3a2-boraphenaleno[2,1,9,8-fghi]pentacene (3e)



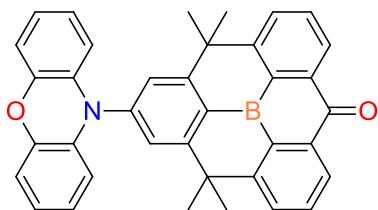
This compound was prepared in a manner analogous to the synthesis of **2e** using **3d** (357 mg, 0.695 mmol) to give a white powder of **3e** (177 mg, 0.345 mmol, yield = 54%). ¹H NMR (CD₂Cl₂): δ 8.77–8.68 (m, 1H), 8.04–7.93 (m, 3H), 7.61 (dd, *J* = 6.4, 3.5 Hz, 2H), 4.89 (s, 1H), 2.20 (s, 6H). The ¹¹B and ¹³C NMR spectra of **3e** could not be obtained due to poor solubility.

2.8. 2-Bromo-4,4,16,16-tetramethyl-4H-3a2-boraphenaleno[2,1,9,8-fghi]pentacene-10(16H)-one (3f)



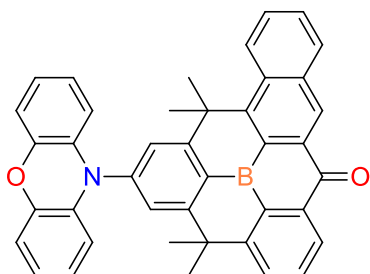
This compound was prepared in a manner analogous to the synthesis of **2f** using **3e** (177 mg, 0.345 mmol) to give a yellow powder of **3f** (138 mg, 0.262 mmol, yield = 76%). ¹H NMR (CD₂Cl₂): δ 9.02 (s, 1H), 8.81 (d, *J* = 8.8 Hz, 1H), 8.27 (dd, *J* = 8.1, 1.1 Hz, 1H), 8.04 (s, 1H), 7.83 (ddd, *J* = 8.6, 6.8, 1.5 Hz, 1H), 7.74 (t, *J* = 7.0 Hz, 1H), 2.24 (s, 6H). The ¹¹B and ¹³C NMR spectra of **3f** could not be obtained due to poor solubility. HRMS (EI): *m/z* [M]⁺ calcd for C₃₃H₂₄BBrO: 526.1109; found: 526.1107.

2.9. Synthesis of PXZBAO (1)



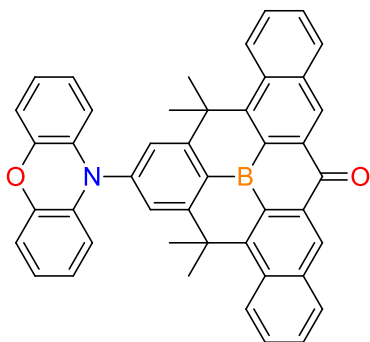
A mixture of BrBCO²⁰ (130 mg, 0.244 mmol), 10*H*-phenoxazine (52.8 mg, 0.288 mmol), Pd₂(dba)₃ (8.8 mg, 0.0096 mmol), [*t*-Bu₃PH][BF₄] (5.6 mg, 0.0192 mmol), and *t*-BuONa (34.6 mg, 0.321 mmol) in toluene (20 mL) was refluxed under a nitrogen atmosphere at 100 °C overnight. After cooling down to room temperature, the reaction mixture was filtered through a pad of Celite and washed with dichloromethane. The filtrate was evaporated under reduce pressure and purified by silica gel column chromatography using ethyl acetate/hexane (1:2, v/v). The product was further recrystallized from a mixed dichloromethane/methanol solution, which afforded a red powder of PXZBAO (1) (107 mg, 0.178 mmol, yield = 73%). ¹H NMR (CD₂Cl₂): δ 8.30 (dd, *J* = 7.6, 0.9 Hz, 1H), 8.05 (dd, *J* = 8.1, 0.9 Hz, 1H), 7.94–7.84 (m, 1H), 7.75 (s, 1H), 6.83–6.60 (m, 3H), 6.12 (dd, *J* = 7.8, 1.5 Hz, 1H), 1.85 (s, 6H). ¹³C NMR (CD₂Cl₂): δ 188.8, 159.8, 155.8, 144.1, 144.0, 138.3, 134.2, 133.8, 131.5, 126.5, 125.5, 123.4, 121.5, 115.4, 113.2, 43.3, 33.1. ¹¹B NMR (CD₂Cl₂): δ 46.2 (s, br). Anal. calcd (%) for C₃₇H₂₈BNO₂: C 83.94, H 5.33, N 2.65%; found: C 83.68, H 5.19, N 3.01. *T*_{d5} = 341 °C. mp = 353 °C.

2.10. Synthesis of PXZBTO (2)



This compound was prepared in a manner analogous to the synthesis of PXZBAO using **2f** (107 mg, 0.214 mmol), 10*H*-phenoxazine (47.1 mg, 0.257 mmol), Pd₂(dba)₃ (7.8 mg, 0.0086 mmol), [*t*-Bu₃PH][BF₄] (5.0 mg, 0.0171 mmol), and *t*-BuONa (30.8 mg, 0.321 mmol), affording a yellow powder of PXZBTO (2) (98 mg, 0.169 mmol, yield = 75%). ¹H NMR (CD₂Cl₂): δ 8.92 (s, 1H), 8.75 (d, *J* = 8.7 Hz, 1H), 8.35 (d, *J* = 7.6 Hz, 1H), 8.23 (d, *J* = 8.1 Hz, 1H), 8.06 (d, *J* = 7.9 Hz, 1H), 7.88 (t, *J* = 7.8 Hz, 1H), 7.81–7.74 (m, 2H), 7.71 (dd, *J* = 13.0, 4.2 Hz, 2H), 6.77–6.60 (m, 6H), 6.11 (dd, *J* = 7.7, 1.5 Hz, 2H), 2.18 (s, 6H), 1.84 (s, 6H). ¹³C NMR (CD₂Cl₂): δ 188.8, 164.8, 158.9, 156.2, 154.4, 144.0, 134.3, 133.8, 132.8, 131.7, 130.0, 128.7, 127.6, 126.9, 125.5, 123.5, 121.5, 115.4, 113.2, 44.5, 43.0, 33.5, 32.2. ¹¹B NMR (CD₂Cl₂): δ 45.8 (s, br). Anal. calcd (%) for C₄₁H₃₀BNO₂: C 84.98, H 5.22, N 2.42; found: C 84.74, H 5.23, N 2.71%. *T*_{d5} = 358 °C. mp = 305 °C.

2.11. Synthesis of PXZBPO (3)



This compound was prepared in a manner analogous to the synthesis of PXZBAO using **3f** (110 mg, 0.209 mmol), 10*H*-phenoxazine (45.9 mg, 0.251 mmol), Pd₂(dba)₃ (8.4 mg, 0.0092 mmol), [*t*-Bu₃PH][BF₄] (5.3 mg, 0.0184 mmol), *t*-BuONa (33.1 mg, 0.345 mmol), affording a yellow powder of PXZBPO (**3**) (88 mg, 0.140 mmol, yield = 70%). ¹H NMR (CD₂Cl₂): δ 9.05 (s, 1H), 8.83 (d, *J* = 8.7 Hz, 1H), 8.29 (d, *J* = 8.0 Hz, 1H), 7.88–7.72 (m, 3H), 6.82–6.65 (m, 3H), 6.18 (dd, *J* = 7.7, 1.6 Hz, 1H), 2.26 (s, 6H). ¹³C NMR (CD₂Cl₂): δ 189.0, 164.0, 154.8, 144.0, 143.6, 137.4, 134.4, 134.1, 132.8, 132.7, 129.9, 128.9, 127.5, 127.3, 126.4, 123.5, 121.4, 115.4, 113.3, 44.1, 32.7. ¹¹B NMR (CD₂Cl₂): δ 43.6 (s, br). Anal. calcd (%) for C₄₅H₃₂BNO₂: C 85.85, H 5.12, N 2.22; found: C 85.38, H 5.05, N 2.54%. *T*_{d5} = 396 °C.

3. X-ray Crystallography

Single crystals of suitable size and quality of PXZBPO (**3**) were coated with Paratone oil and mounted onto a glass capillary. Diffraction data were obtained at 193 K. The crystallographic measurements were performed on a Bruker SMART Apex II CCD area detector diffractometer with graphite-monochromated Mo-K α radiation ($\lambda = 0.71073$ Å). The structures were solved by direct methods³ and refined by full-matrix least-squares fitting on F^2 using SHELXL-2014.⁴ All non-hydrogen atoms were refined with anisotropic displacement parameters. The carbon-bound hydrogen atoms were introduced at calculated positions and all hydrogen atoms were treated as riding atoms with an isotropic displacement parameter equal to 1.2 times that of the parent atom.

4. Photophysical Measurements

UV/Vis absorption and photoluminescence (PL) spectra were recorded on a Varian Cary 100 and FLS1000 spectrophotometer, respectively. Dilute sample solutions (typically 2.0×10^{-5} M) were prepared in a glovebox at ambient conditions. Photoluminescence quantum yields (PLQYs) were measured on an absolute PL quantum yield spectrophotometer (Quantaaurus-QY C11347-11, Hamamatsu Photonics) equipped with a 3.3-inch integrating sphere. Transient PL decays were measured on a FLS1000 spectrophotometer (Edinburgh Instruments) with a time-correlated single-photon counting (TCSPC) method using an EPL-375 picosecond pulsed

diode laser ($\lambda_{\text{exc}} = 375 \text{ nm}$). PLQYs of prompt (Φ_{p}) and delayed (Φ_{d}) fluorescence were estimated from the prompt and delayed components of the transient decay curves, respectively. The temperature-dependence of PL decay was obtained with an OptistatDNTM cryostat (Oxford Instruments).

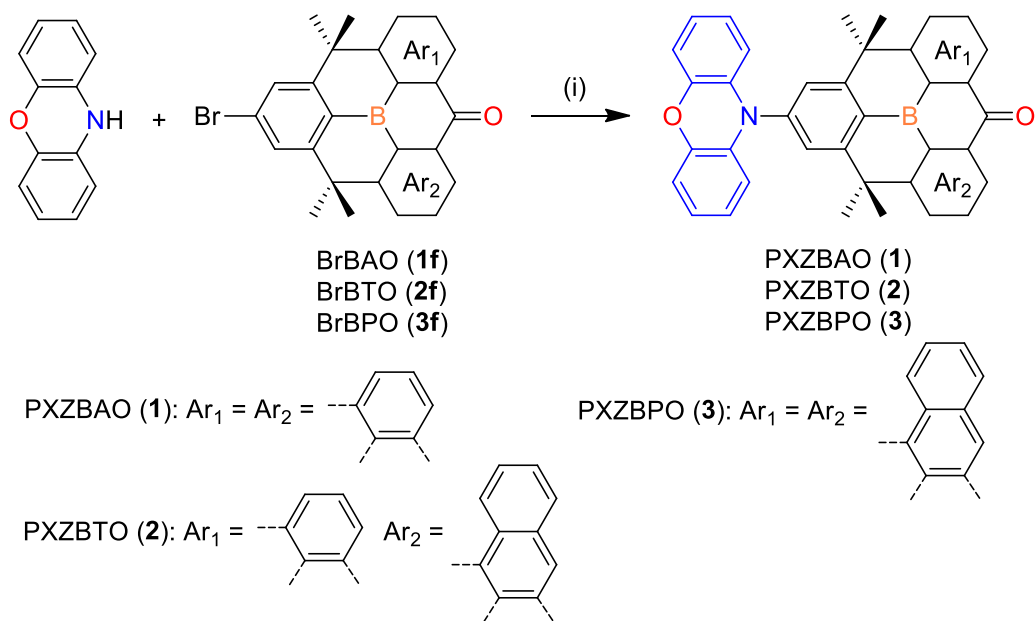
5. Cyclic Voltammetry

Cyclic voltammetry measurements for electrochemical oxidation were carried out in dichloromethane ($5 \times 10^{-4} \text{ M}$) with a three-electrode cell configuration consisting of platinum working and counter electrodes and an Ag/AgNO₃ (0.01 M in CH₃CN) reference electrode at room temperature. Tetra-*n*-butylammonium hexafluorophosphate (0.1 M) was used as the supporting electrolyte. The oxidation potentials were recorded at a scan rate of 100 mV/s and are reported with reference to the ferrocene/ferrocenium (Fc/Fc⁺) redox couple.

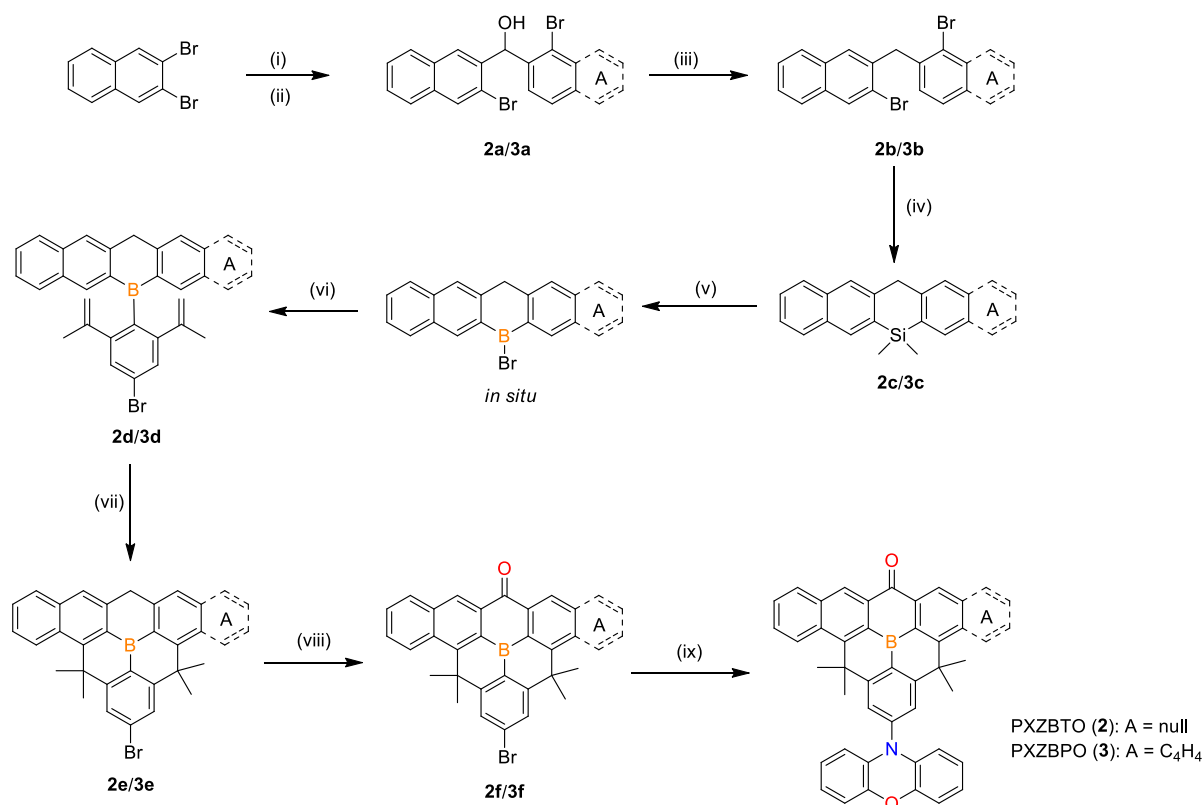
III. RESULT AND DISCUSSION

1. Synthesis and Characterization

A series of boron-carbonyl hybrid acceptor connected with phenoxazine donor were prepared according to **Scheme 1**. The Br-BCO (**1f**) acceptor was prepared based on the reported literature.²⁰ The BTO-Br (**2f**) and BPO-Br (**3f**) was prepared according to full synthetic experimental in **Scheme 2**.



Scheme 1 . Conditions : (i) Pd₂(dba)₃, [*t*-Bu₃PH][BF₄], *t*-BuONa, toluene, 110 °C, 2 d.



Scheme 1 . Conditions : (i) *i*-PrMgCl.LiCl, THF, $-15\text{ }^{\circ}\text{C}$, 2 h; (ii) bromobenzaldehyde (**2a**) / ethyl formate (**3a**); (iii) HI, acetic acid, reflux; (iv) *n*-BuLi, THF, $-78\text{ }^{\circ}\text{C}$ (**2c**) / ether, $0\text{ }^{\circ}\text{C}$ (**3c**), 3 h then Me₂SiCl₂, THF, $-78\text{ }^{\circ}\text{C}$ (**2c**) / ether, $0\text{ }^{\circ}\text{C}$ (**3c**), 12 h; (v) BBr₃, neat; (vi) *n*-BuLi, toluene, $0\text{ }^{\circ}\text{C}$, 3 h, then 2,6-di(propen-2-yl)phenyl-lithium, toluene, $0\text{ }^{\circ}\text{C}$; (vii) Sc(OTf)₃, 1,2-DCE, reflux; (viii) PCC, dichloromethane, reflux, 12 h; (ix) 10*H*-Phenoxazine, Pd₂(dba)₃, [*t*-Bu₃PH][BF₄], *t*-BuONa, toluene, $110\text{ }^{\circ}\text{C}$, 2 d.

Compound **2a** and **3a** were initially synthesized from 2,3-dibromonaphthalene as a starting material was subjected to the Grignard reagent exchange conditions and quenched with either 2-bromobenzaldehyde or ethyl formate to give diaryl methanol derivatives of **2a** and **3a**, respectively. The alcohols of **2a** and **3a** were reduced with hydroiodic acid in acetic acid at reflux conditions resulting compound **2b** and **3b**. The formation of Grignard reagents from **2a/3a-2b/3b**.^{21,22} followed by addition of Me₂SiCl₂ resulting silicon-bridged boratetracene (**2c**) and borapentacene (**3c**), respectively. The silicon-boron exchange reaction of **2c/3c** with excess neat BBr₃ proceeded smoothly, connected with the salt 2,6-di(propen-2-yl)phenyl-lithium resulting compound **2d/3d**. Further, compound **2d/3d** were proceeded through intramolecular Friedel-Crafts cyclization in the presence of Sc(OTf)₃ resulting **2e/3e**, followed by oxidation with PCC oxidant in refluxing dichloromethane produced **2f/3f**. Finally, **1f-3f** acceptor were

proceed through Buchwald-Hartwig coupling amination reaction with 10*H*-Phenoxazine donor generate the full compounds of PXZBAO (**1**), PXZBTO (**2**), and PXZBPO (**3**). All final compounds were characterized by multinuclear NMR spectroscopy (**Figure 7-17**) and elemental analysis.

The ¹H NMR spectra of all compounds exhibits singlet of CH₃ group (δ 1.86 ppm) and (δ 2.26 ppm) substituted at the same two dimethyl bridge of BAO and BPO respectively, and singlet of CH₃ group (δ 1.84 and 2.18 ppm) substituted at the two dimethyl bridge from the asymmetry of BTO. The ¹³C NMR spectra of all compounds shows the peak in the downfield region (δ 188.8–189.0 ppm) indicating from carbonyl group of the acceptor. As for ¹¹B, a tri-coordinated boron center was detected as a broad resonance signal at δ 43.6 – 48.2 ppm for all compounds, which is consistent with the presence of trigonal planar boron centre from BCO group. The single crystal structure was confirmed by an X-ray diffraction study performed on PXZBPO (**Figure 19**). A twisted structure of the compound was confirmed by a large dihedral angle of 83.47° for \angle PXZ-BPO. The detailed crystallographic data and the selected bond lengths and angles are given in **Table 1 and 2**. Furthermore, from TGA analysis (**Figure 19**) showed this series have high thermal stability, giving Td₅ value of 341 °C, 358 °C, and 396 °C for PXZBAO, PXZBTO, and PXZBPO respectively.

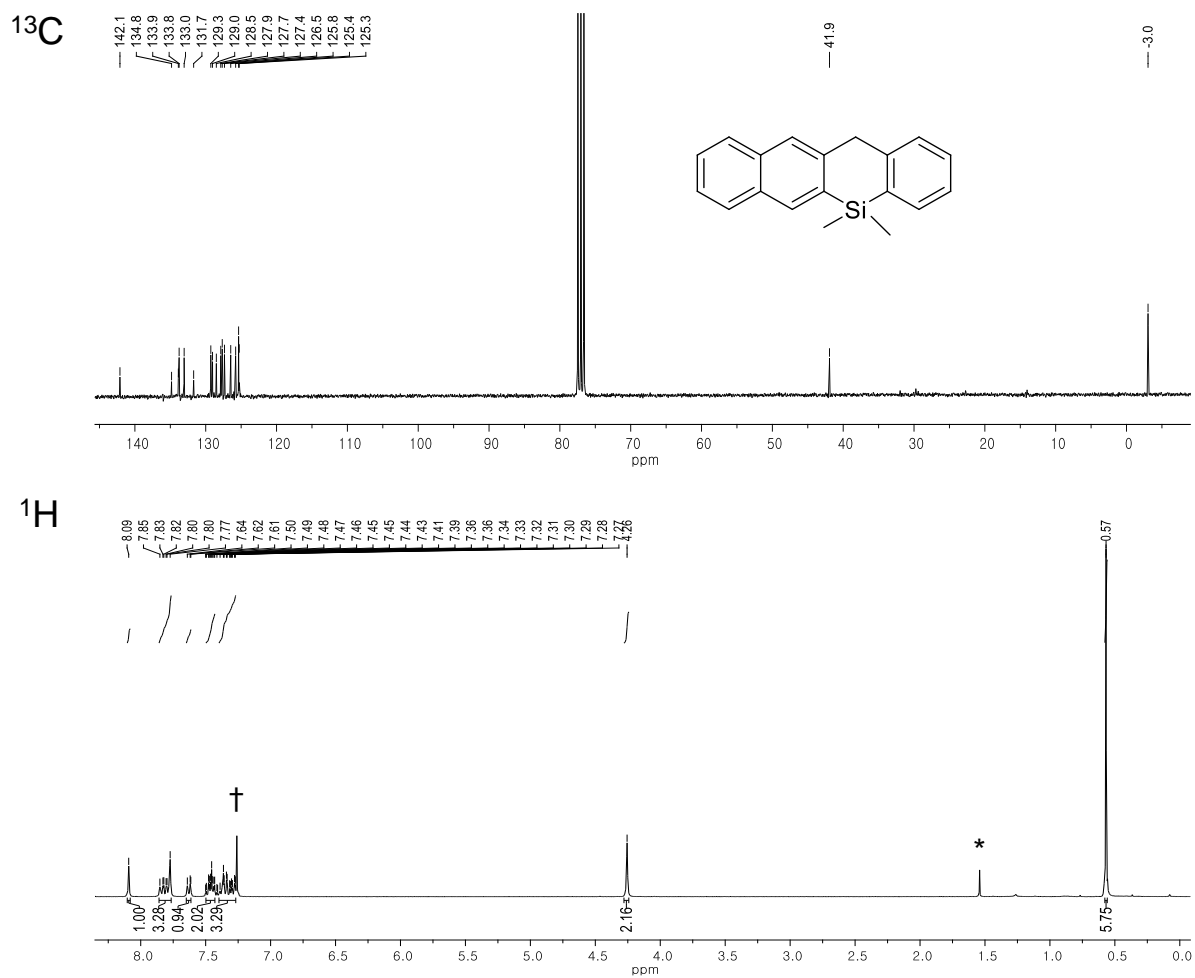


Figure 7. ¹³C (top) and ¹H (bottom) NMR spectra of 2c in CDCl₃ (* from water and † from residual CHCl₃).

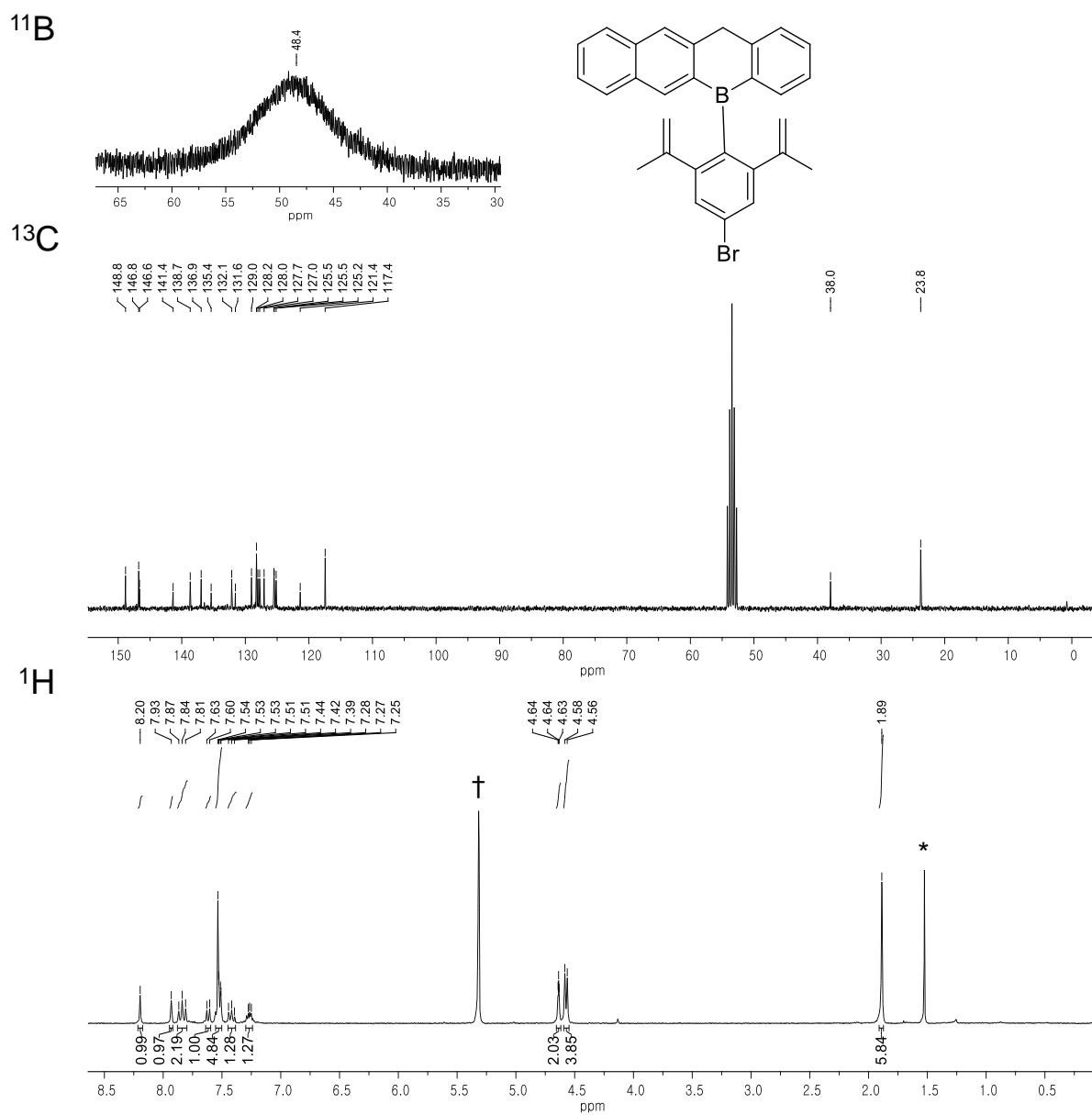


Figure 8. ¹¹B (top), ¹³C (middle), and ¹H (bottom) NMR spectra of 2d (* from water and † from residual CHDCl₂).

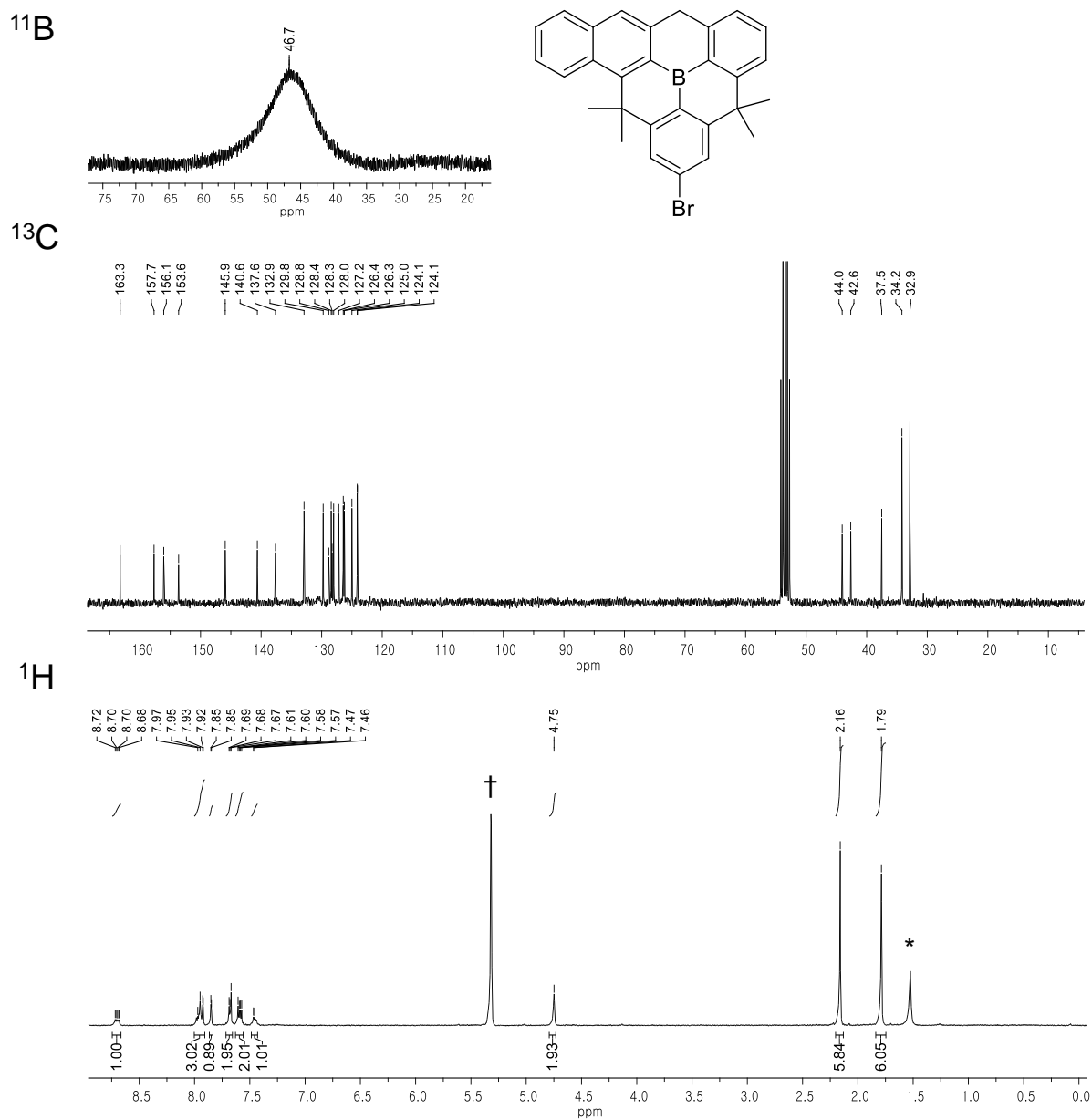


Figure 9. ¹¹B (top), ¹³C (middle), and ¹H (bottom) NMR spectra of 2e (* from water and † from residual CHDCl₂).

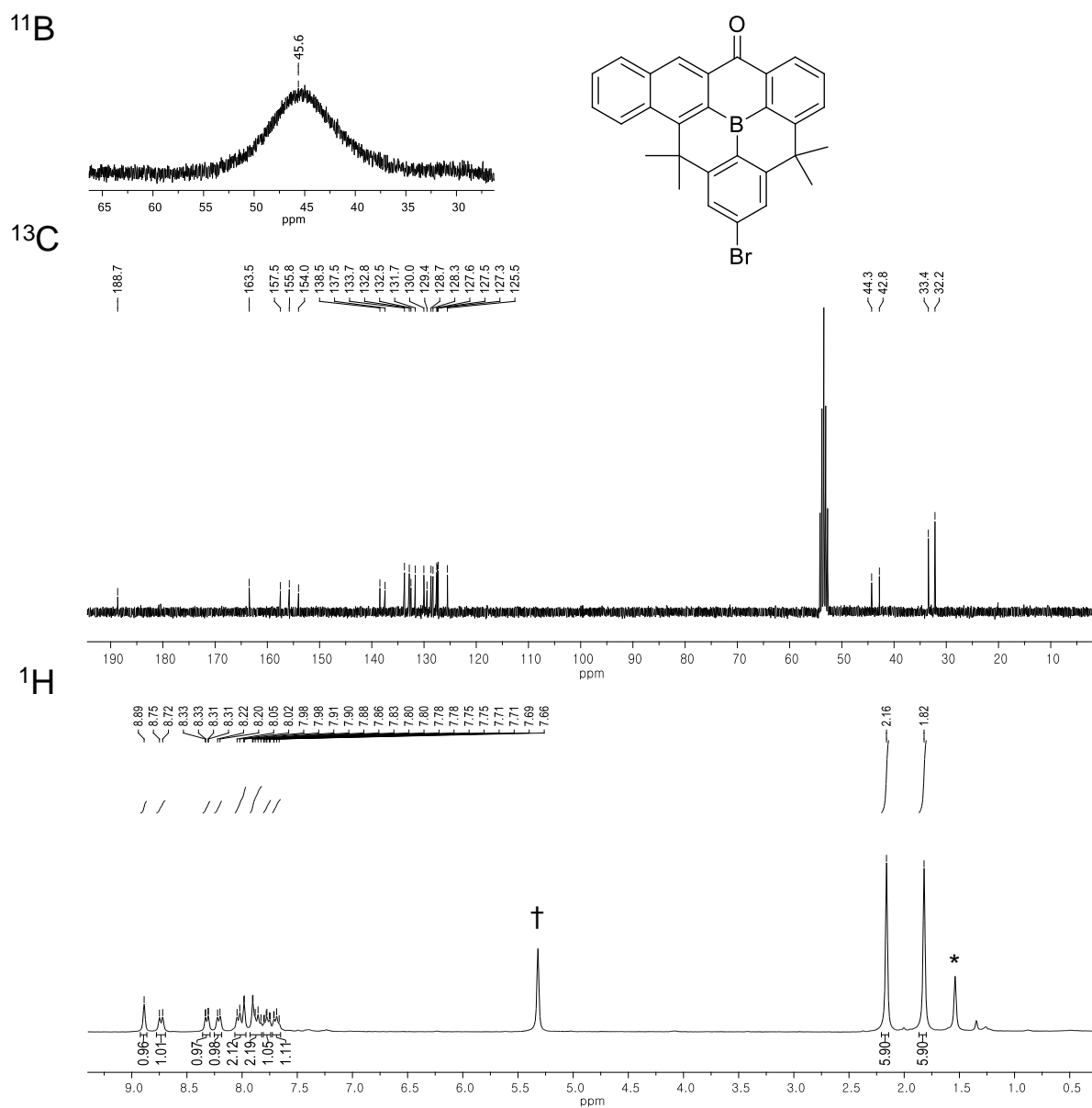


Figure 10. ¹¹B (top), ¹³C (middle), and ¹H (bottom) NMR spectra of 2f (* from water and † from residual CHDCl₂).

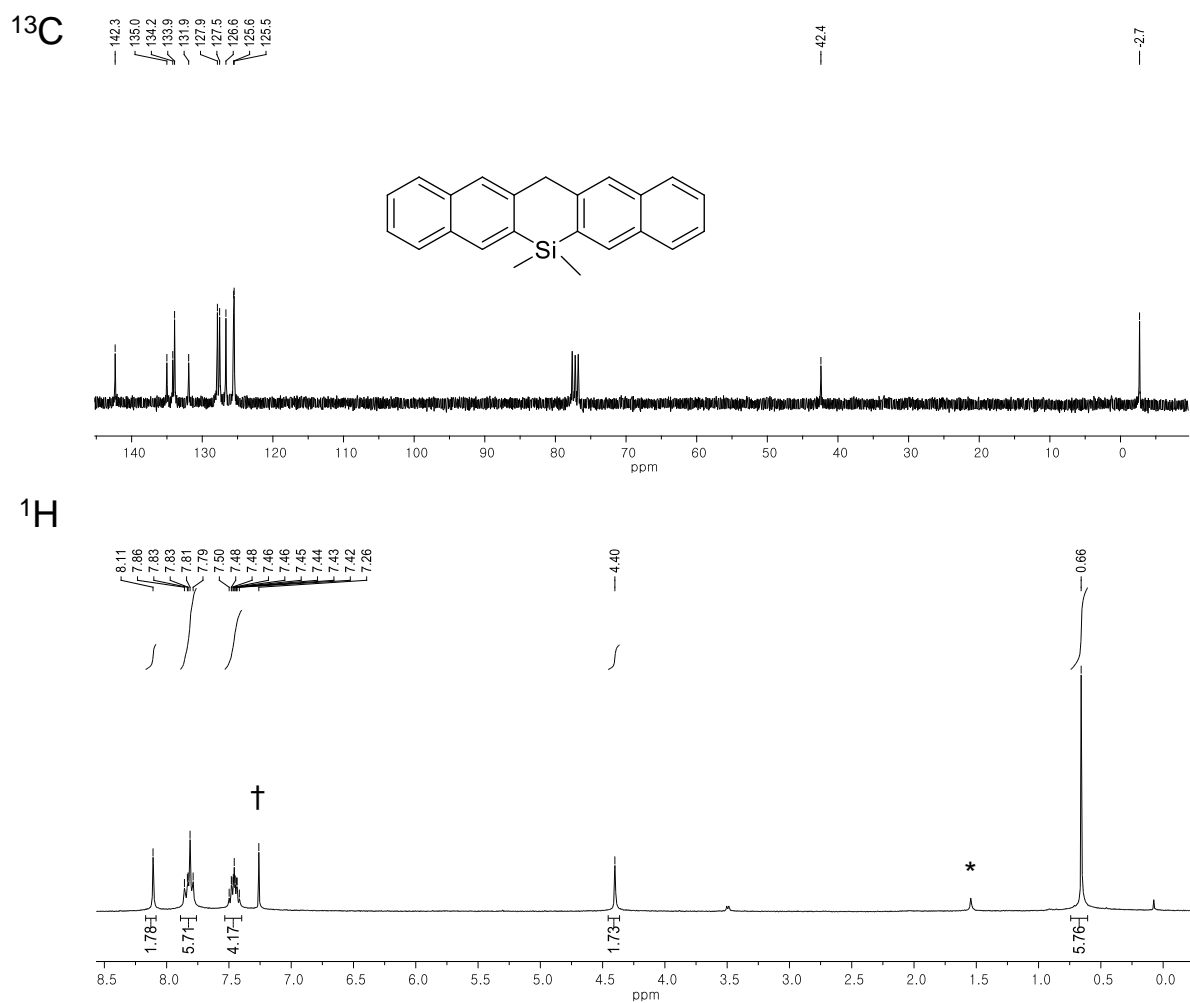


Figure 11. ¹³C (top) and ¹H (bottom) NMR spectra of 3c (* from water and † from residual CHCl₃).

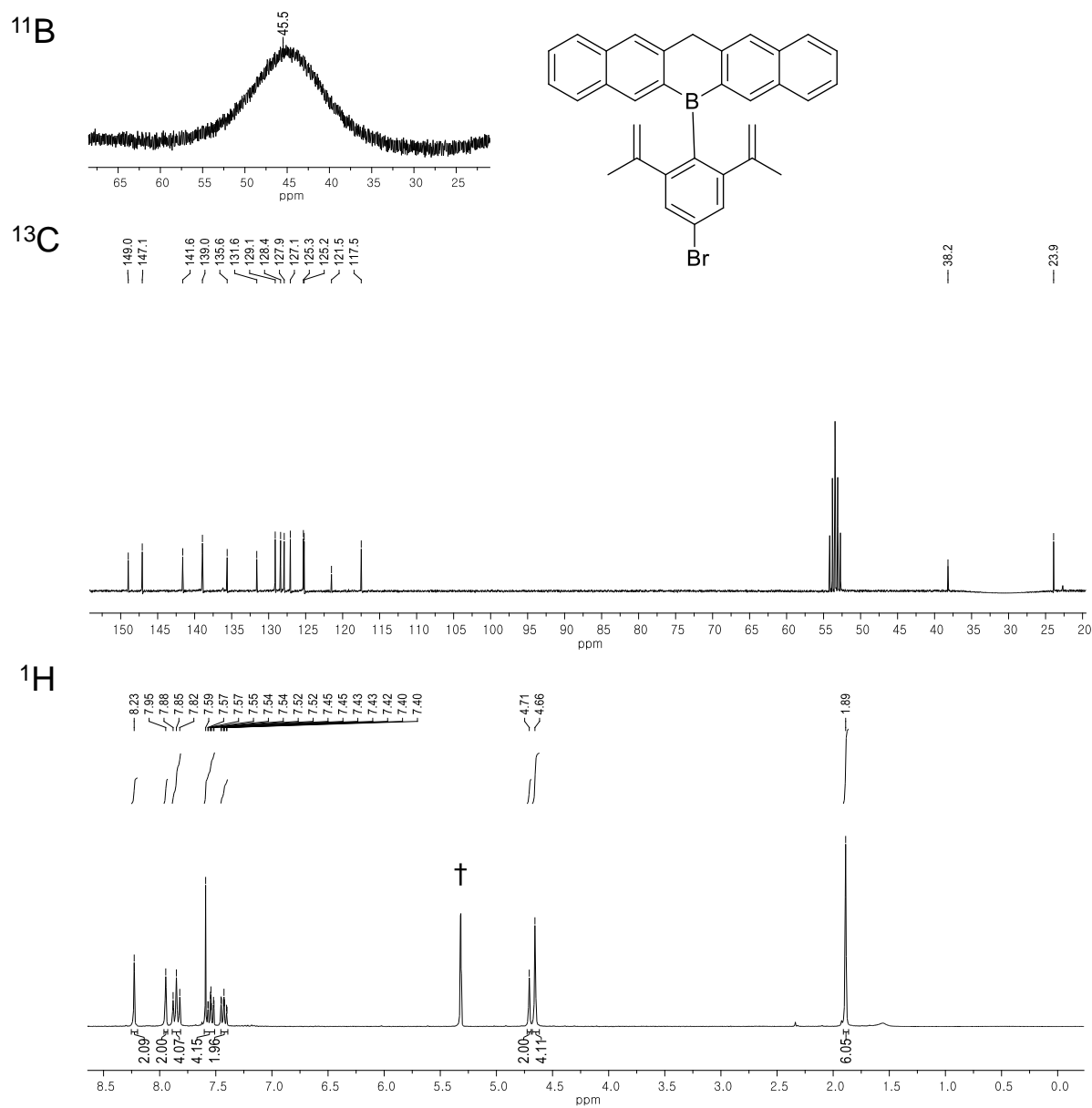


Figure 12. ¹¹B (top), ¹³C (middle), and ¹H (bottom) NMR spectra of 3d in CD₂Cl₂ (* from water and † from residual CHDCl₂).

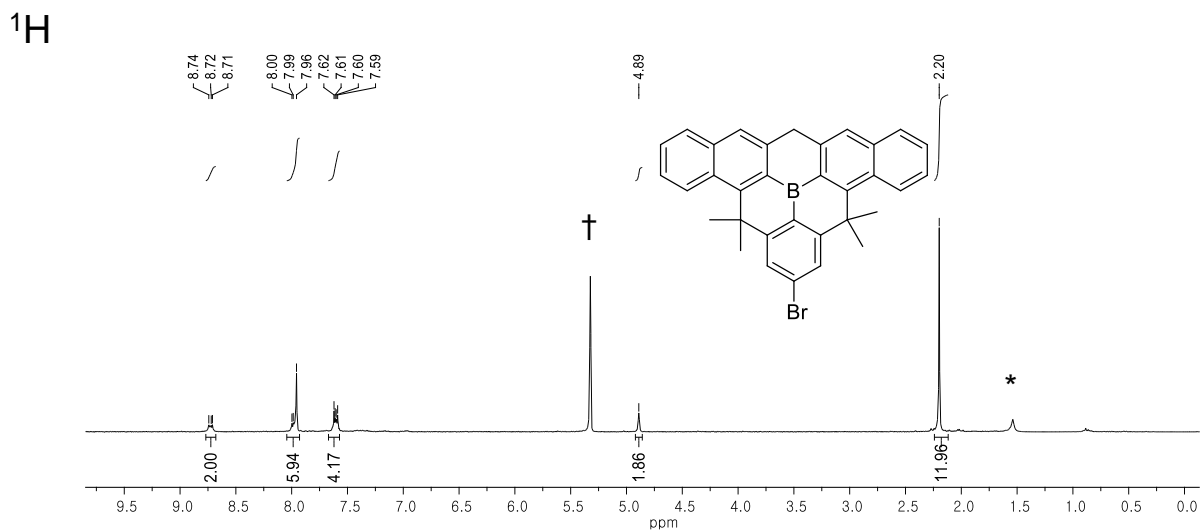


Figure 13. ^1H NMR spectra of 3e in CD_2Cl_2 (* from water and † from residual CH_2Cl_2).



Figure 14. ^1H NMR spectra of 3f in CD_2Cl_2 (* from water and † from residual CH_2Cl_2).

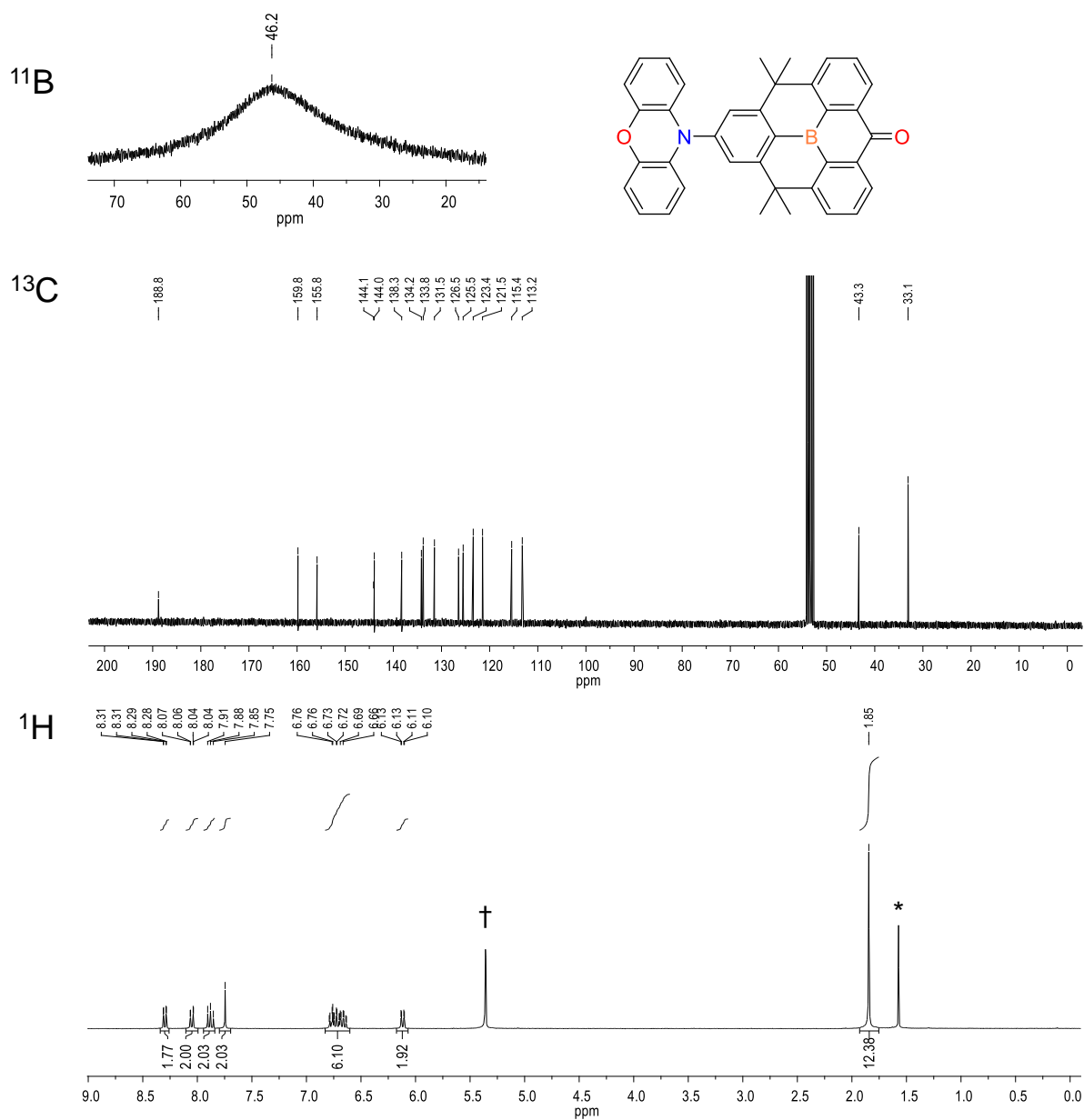


Figure 15. ¹¹B (top), ¹³C (middle), and ¹H (bottom) NMR spectra of PXZBAO (1) (* from water and † from residual CHDCl₂).

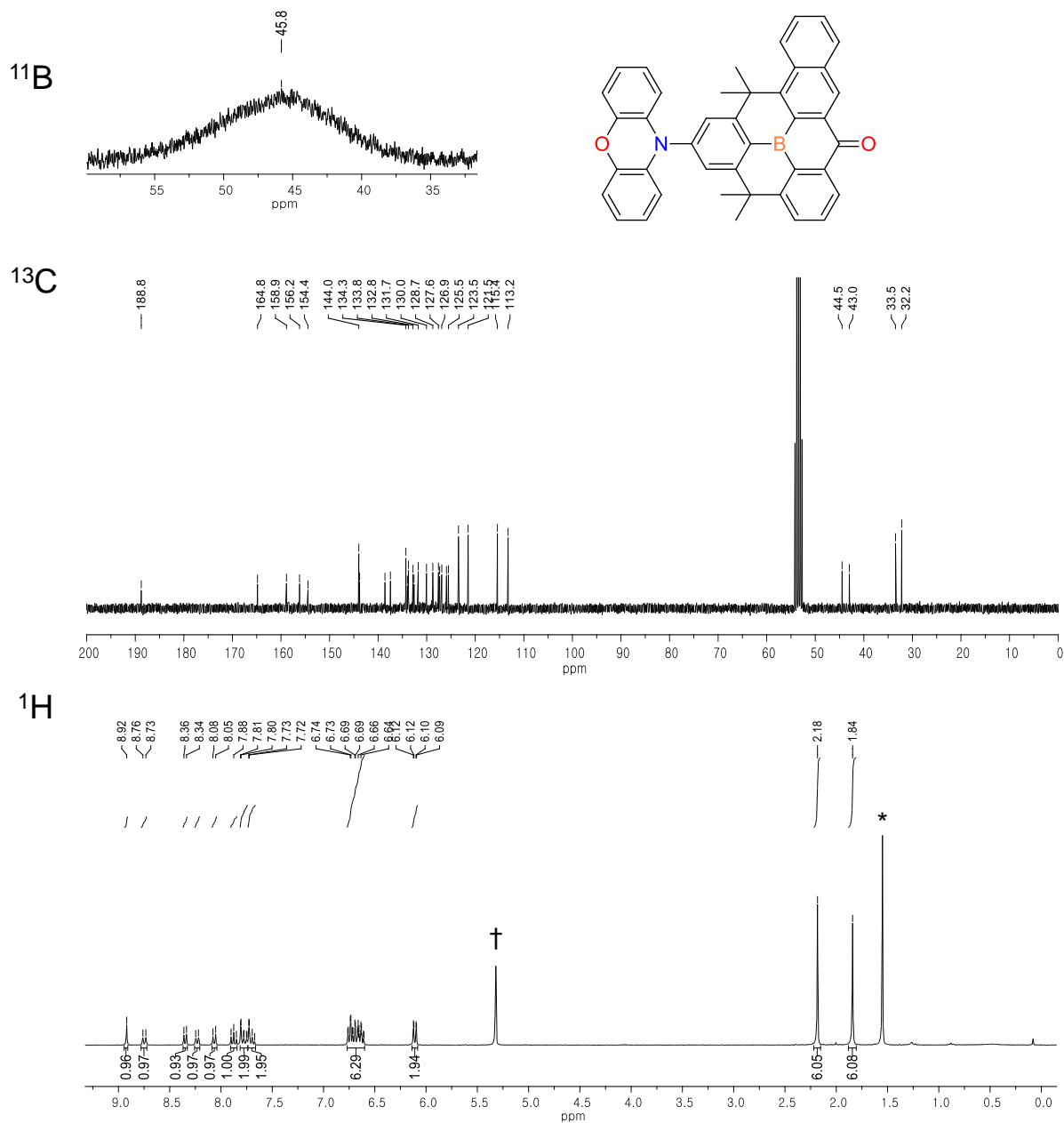


Figure 16. ¹¹B (top), ¹³C (middle), and ¹H (bottom) NMR spectra of PXZBTO (2) (* from water and † from residual CHDCl₂).

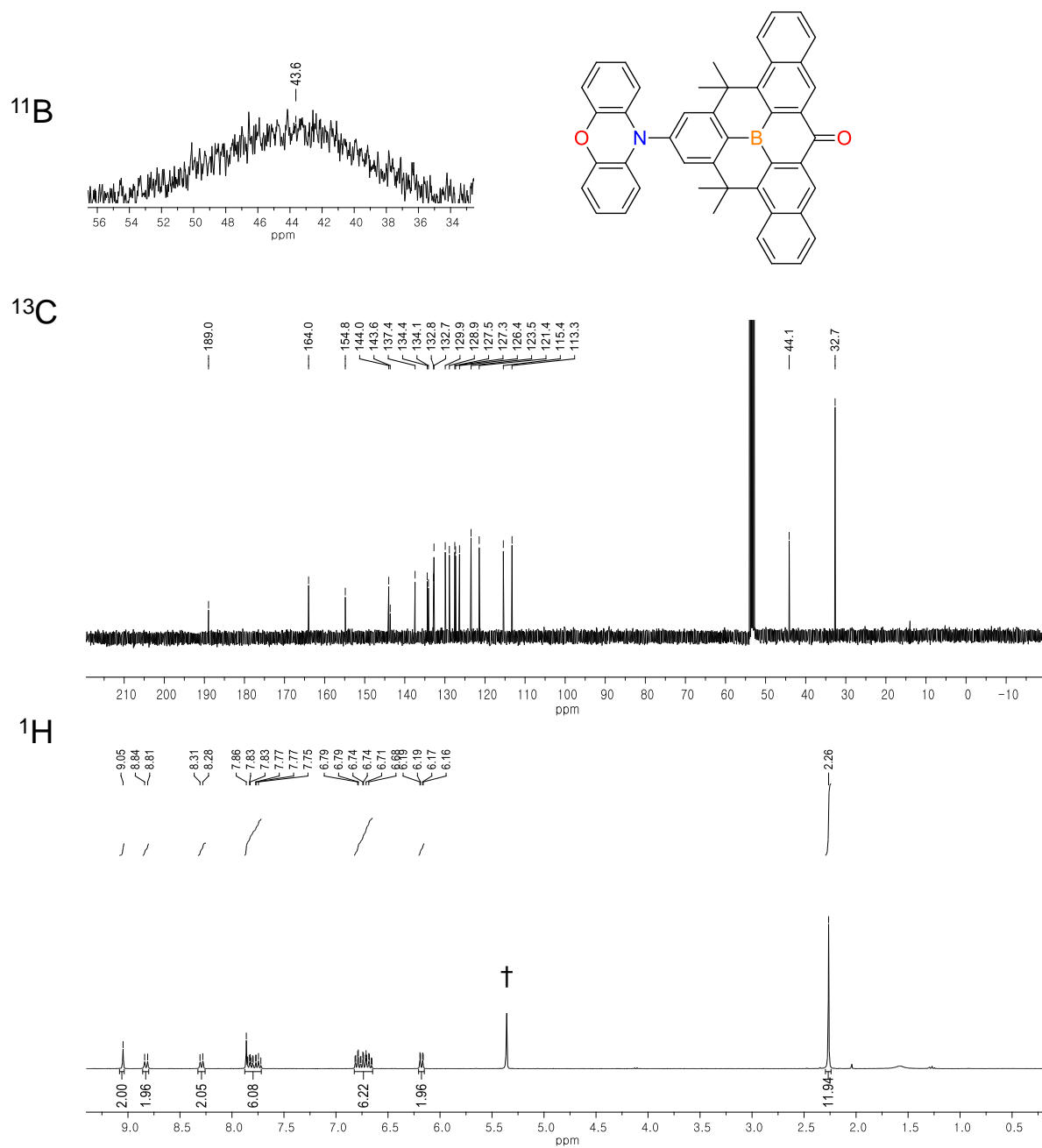


Figure 17. ¹¹B (top), ¹³C (middle), and ¹H (bottom) NMR spectra of PXZBPO (3) († from residual CHDCl₂).

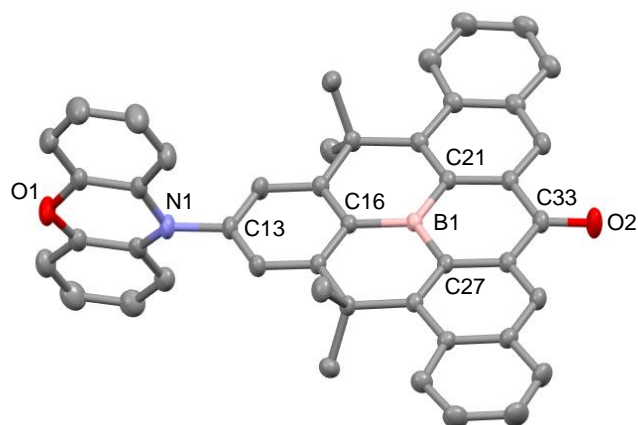


Figure 18. X-ray crystal structure of PXZBPO (3) (50% thermal ellipsoids). H atoms are omitted for clarity. Color code: blue = nitrogen; brown = boron; red = oxygen.

Table 1. Selected bond lengths (Å) and angles (°) of PXZBPO.

PXZBPO	
Lengths(Å)	
B(1)-C(16)	1.510(3)
B(1)-C(21)	1.529(3)
B(1)-C(27)	1.530(3)
N(1)-C(13)	1.441(2)
C(33)-O(2)	1.229(2)
Angles (°)	
C(16)-B(1)-C(21)	119.27(16)
C(16)-B(1)-C(27)	119.13(16)
C(21)-B(1)-C(27)	121.57(16)

Table 2. Crystallographic data and parameters for PXZBPO.

	PXZBPO
Formula	C ₄₅ H ₃₂ BNO ₂
formula weight	629.55
crystal system	Monoclinic
space group	P2 ₁ /c
<i>a</i> (Å)	14.1980(6)
<i>b</i> (Å)	19.6765(8)
<i>c</i> (Å)	12.5258(5)
α (°)	90
β (°)	98.300(2)
γ (°)	90
<i>V</i> (Å ³)	3462.6(2)
<i>Z</i>	4
ρ_{calc} (g cm ⁻³)	1.370
μ (mm ⁻¹)	0.231
<i>F</i> (000)	1488
<i>T</i> (K)	193
<i>hkl</i> range	-18 → 18, -26 → 26, -16 → 16
measd reflns	57641
unique reflns [<i>R</i> _{int}]	8614(0.0563)
reflns used for refinement	8614
refined parameters	482
<i>R</i> 1 ^{<i>a</i>} (<i>I</i> > 2σ(<i>I</i>))	0.0716
w <i>R</i> 2 ^{<i>b</i>} all data	0.2126
GOF on <i>F</i> ²	1.043
ρ_{fin} (max/min) (e Å ⁻³)	0.498/-1.356

^{*a*} $R1 = \frac{\sum ||F_o| - |F_c||}{\sum |F_o|}$. ^{*b*} $wR2 = \frac{\{[\sum w(F_o^2 - F_c^2)^2]/[\sum w(F_o^2)^2]\}^{1/2}}$

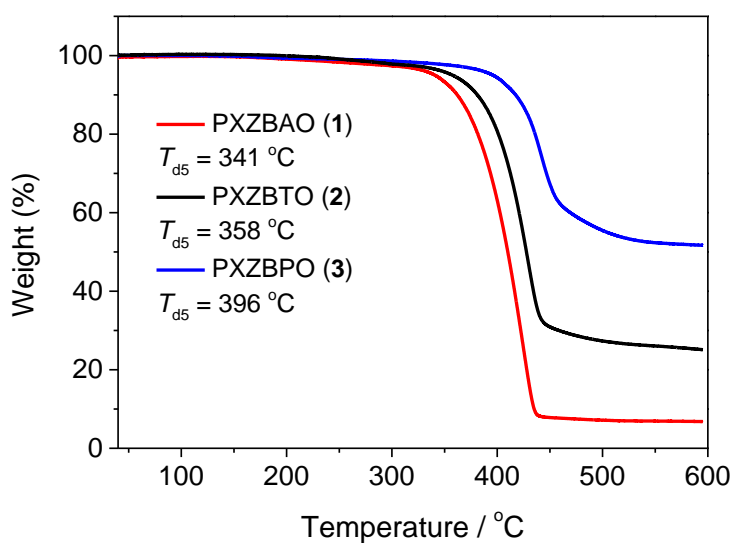


Figure 19. TGA Curves of PXZBAO (1), PXZBTO (2), and PXZBPO (3).

2. Photophysical Properties

The photophysical properties of all compounds including UV/Vis absorption and photoluminescence (PL) spectra, were measured in oxygen-free toluene ($(2.0 \times 10^{-5} \text{ M})$) at 298 K. (**Figure 20** and **Table 3**). The strong absorptions in the high energy region of 250–350 nm can be assigned from $\pi-\pi^*$ transition of the phenoxazine donor and triarylboron-centered $\pi-p_{\pi}(\text{B})$ charge transfer (CT) transition.^{23,24} The broad low-energy absorptions (ca. 420–500 nm) can be resulted from intramolecular charge transfer (ICT) transition from the donor to acceptor moieties.²⁴ The PL spectra showed blue-shifted emission as the number of naphthyl ring increased (PXZBAO = 619 nm, PXZBTO = 594 nm, PXZBPO = 575 nm). As for PLQY, PXZBPO and PXZBTO exhibited high PLQY (PXZBPO = 1.00, PXZBTO = 0.77) in oxygen free toluene. All compounds have the large decrease of the PLQY in air-saturated toluene owing to the quenching of the T_1 states by triplet oxygen. The transient PL decay curves obtained at 298 K showed two decay components, i.e., the nanosecond-range prompt (τ_p) and microsecond-range delayed (τ_d) components. The lifetimes of the delayed components (τ_d) were relatively short for all compounds ($\tau_d < 2 \mu\text{s}$) (**Figure 22**). The intensity of the delayed emission was gradually increase with increasing temperature from 80 K to 295 K confirms that the observed delayed emission can be assigned to TADF (**Figure 23**). The ΔE_{ST} values were determined experimentally from the fluorescence and phosphorescence spectra at 77 K and were found to be in the range of 11.5–51 meV, which are confirms characteristic of strong TADF properties (**Figure 24**, **Table 4**).

Photophysical properties were also measured in mCBP host film doped with 5% weight (5 wt%) of compounds (**Figure 21**). Similar with the solution, the blue-shifted emission was observed as the number of the naphthyl ring increased. All the compounds were blue-shifted of ca.10-12 nm compared to solution data. This could be affected from the highly rigidity of compounds and also the rigid matrix of mCBP film. All compounds in film exhibit moderate to high PLQY in a value of 0.55-1.00.

Nucleus Independent Chemical Shifts (NICS) were performed to identify the aromaticity character of the molecules. The NICS values were reported with reversed signs, negative values denoted aromaticity and positive values denoted antiaromaticity. NICS (1) demonstrated the values 1Å above the molecular plane.²⁵ Based on the **Figure 25**, the antiaromaticity character was increased as the number of the naphthyl group increased. This result supported that as the number of the naphthyl group increased from compound **1-3**, the emission wavelength will undergo to the blue-shifted.

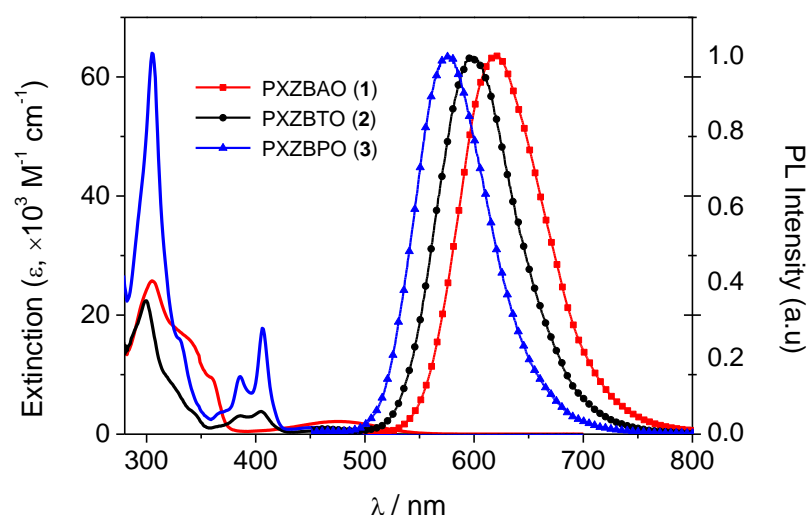


Figure 20. UV/vis absorption (left) and PL spectra (right) of PXZBAO (**1**), PXZBTO (**2**), and PXZBPO (**3**) in toluene (2.0×10^{-5} M) at 298 K.

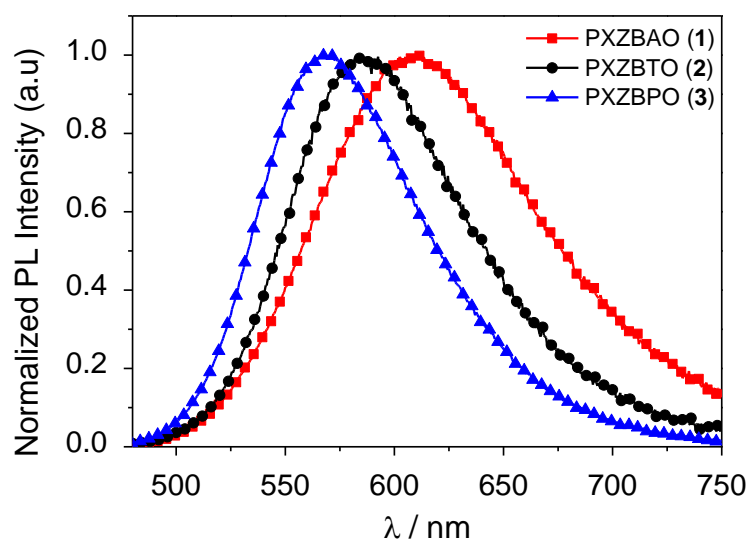


Figure 21. PL spectra of PXZBAO (1), PXZBTO (2), and PXZBPO (3) in 5 wt% mCBP at 298 K.

Table 3. Photophysical properties of PXZBAO, PXZBTO, and PXZBPO.

Compound	λ_{abs}^a [nm]	λ_{PL} [nm]		Φ_{PL} (%)		τ_{p} [ns (%)] ^c		τ_{d} [μs (%)] ^d	
		Toluene ^a	5 wt% in mCBP	Toluene ^b (N ₂ /air)	5 wt% in mCBP	Toluene	5 wt% in mCBP	Toluene	5 wt% in mCBP
PXZBAO	305, 321, 356, 476	619	609	29/9	55	24.79 (17.01)	38.74 (77.50)	0.98 (82.99)	1.03 (22.50)
PXZBTO	298, 344, 384, 405	597	586	74/19	97	44.46 (45.77)	56.42 (73.83)	1.17 (54.21)	1.45 (26.17)
PXZBPO	306, 331, 385, 406	574	568	100/25	99	52.92 (45.94)	57.85 (71.95)	1.43 (54.06)	1.76 (28.05)

^{a)} In oxygen-free toluene at 298 K (2.0×10^{-5} M); ^{b)} Absolute photoluminescence quantum yields (PLQYs) in oxygen-free (N₂) and air-saturated (air) toluene at 298 K; ^{c)} PL lifetimes of prompt (τ_{p}) decay components for the air-saturated toluene solutions at 298 K. The estimated prompt (Φ_{PF}) portions (%) in transient decay curves are given in parentheses. ^{d)} PL lifetimes of delayed (τ_{d}) decay components (oxygen-free toluene solutions and film at 298 K). The estimated delayed (Φ_{DF}) portions (%) in transient decay curves are given in parentheses.

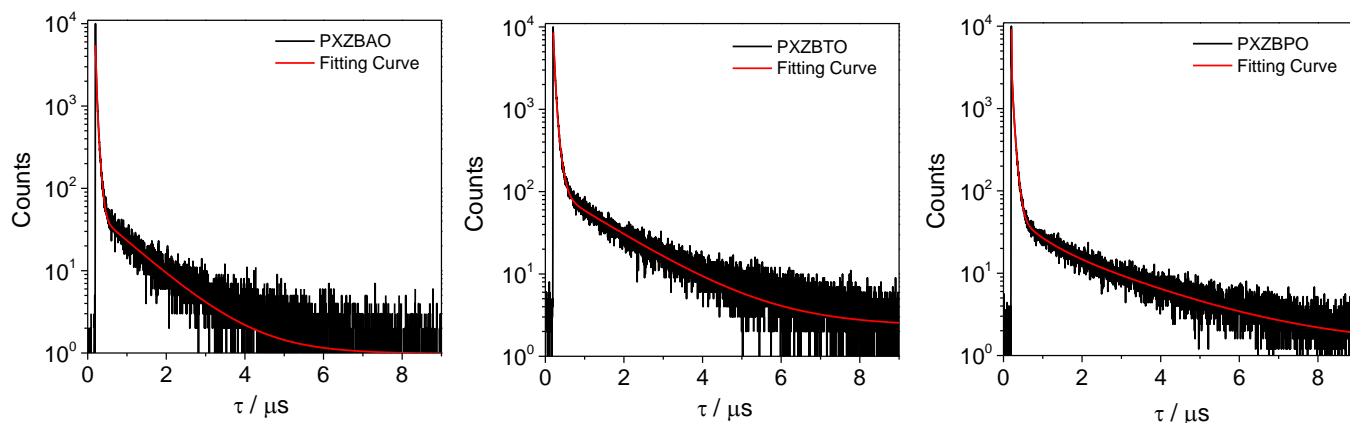


Figure 22. Transient PL decay curves of PXZBAO (left), PXZBTO (middle), PXZBPO (right) in oxygen-free toluene at 298 K.

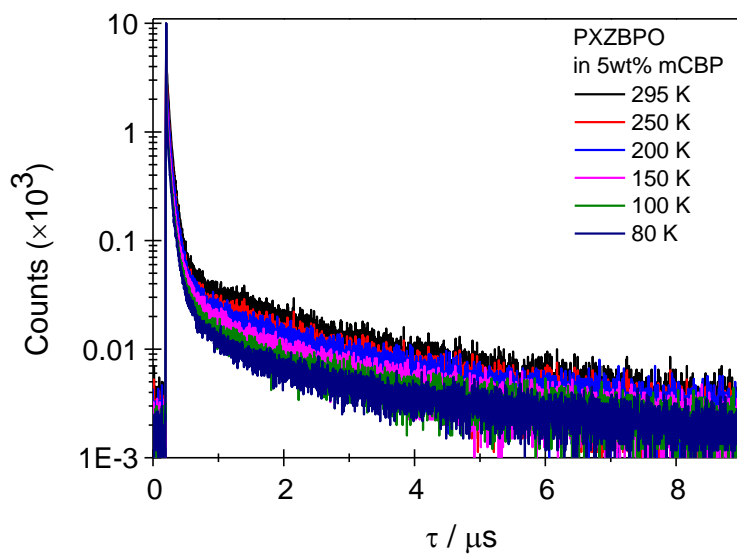


Figure 23. The temperature dependant of the transient PL decay from 80 to 295 K (PXZBPO).

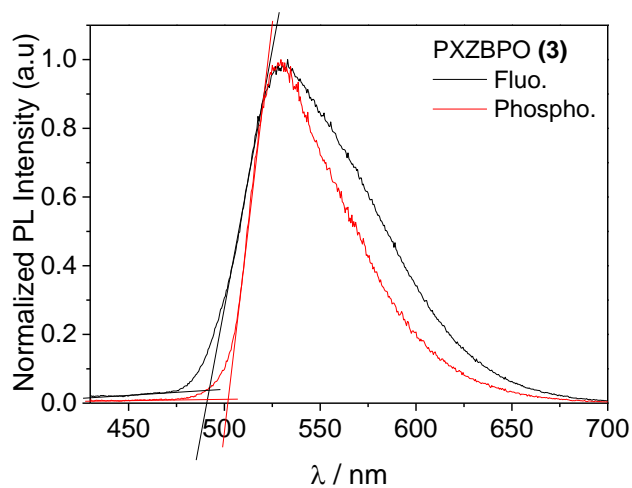
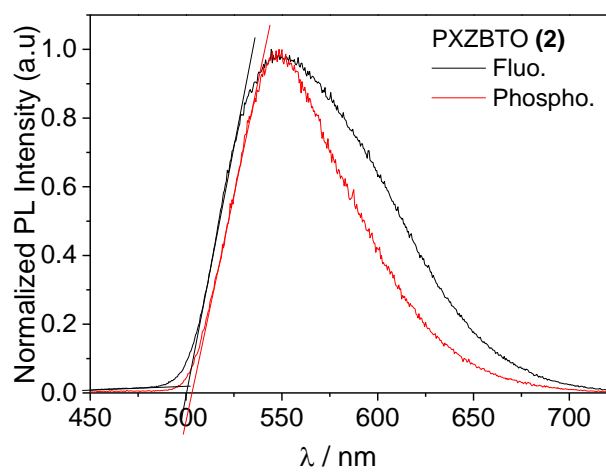
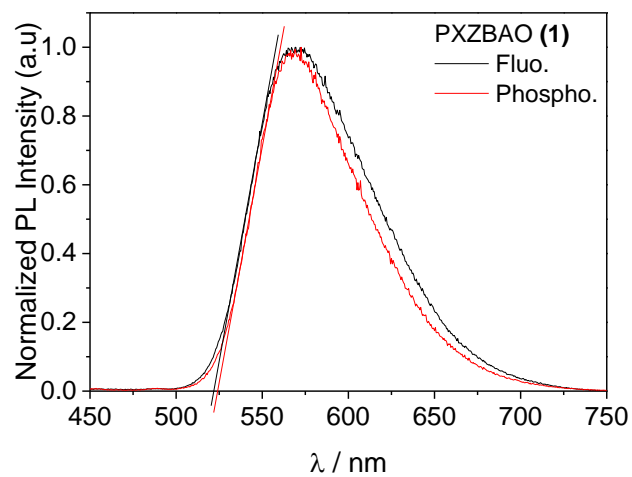
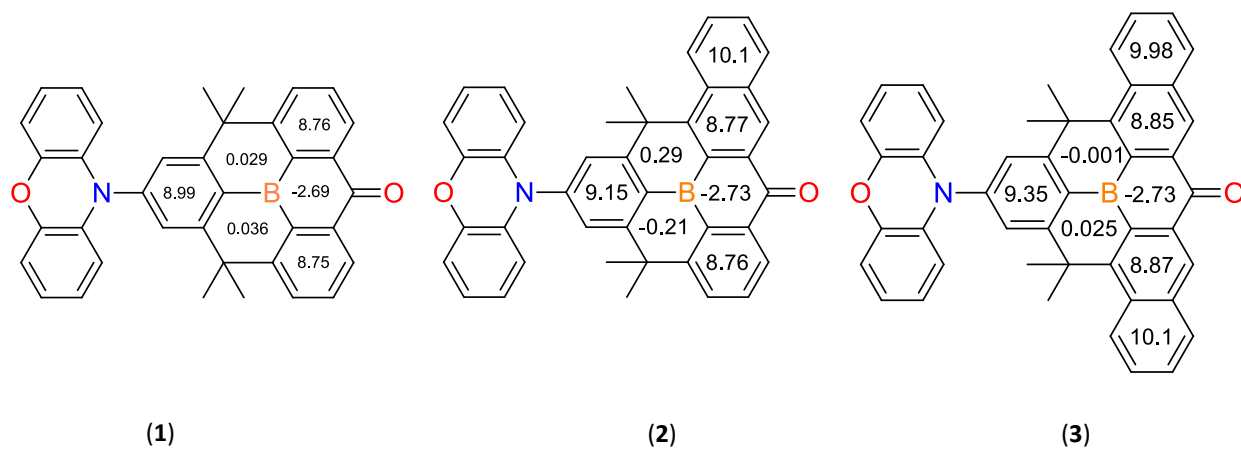


Figure 24. Fluorescence and phosphorescence spectra of PXZBAO (top), PXZBTO (middle), and PXZBPO (bottom) in toluene at 77 K.

Table 4. Photophysical data of PXZBAO, PXZBTO, and PXZBPO at 77 K.

Compound	λ_{PL} [nm]	$E_{\text{S}}/E_{\text{T}}^a$ [eV]	ΔE_{ST}^b [eV]
PXZBAO	570	2.377/2.366	0.011
PXZBTO	548	2.477/2.462	0.015
PXZBPO	530	2.520/2.469	0.051

^{a)} E_{S} and E_{T} were calculated from the onset of fluorescence and phosphorescence spectra respectively. ^{b)} $\Delta E_{\text{ST}} = E_{\text{S}} - E_{\text{T}}$.

**Figure 25.** NICS (Nucleus-Independent Chemical Shift) value of PXZBAO (1), PXZBTO (2), PXZBPO (3) in toluene, calculated at the PBE0/6-311++G(d,p) level of theory.

3. Electrochemical Properties

The electrochemical properties of PXZBAO, PXZBTO, and PXZBPO were obtained by cyclic voltammetry to investigate the character of the frontier orbitals molecule. The half-wave oxidation potentials (E_{ox} versus Fc/Fc^+) were 0.34 (PXZBAO), 0.33 (PXZBTO) and 0.33 (PXZBPO), correspond to the reversible oxidation from donor moieties. PXZBAO, PXZBTO, and PXZBPO are estimated to have identical HOMO value due to the same moieties of phenoxazine donor. Consequently, their HOMO energy levels determined from the half-wave oxidation potentials were -5.14 eV, -5.13 eV, and -5.13 eV. All reduction potentials estimated from the optical band gap (E_g) and the HOMO levels, giving their calculated LUMO energy levels were -2.86 eV (PXZBAO), -2.77 (PXZBTO), and -2.71 (PXZBPO) respectively (**Figure 26**, **Table 5**).

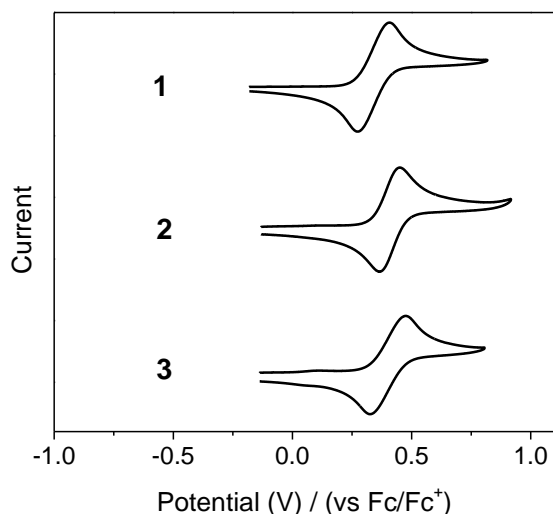


Figure 26. Cyclic voltammograms of PXZBAO (1), PXZBTO (2), and PXZBPO (3) showing oxidation (5.0×10^{-4} M in CH_2Cl_2 , scan rate = 100 mV/s).

Table 5. Cyclic Voltammetry Data of PXZBAO, PXZBTO, and PXZBPO.

	E_{ox} (V) ^a	E_g (eV) ^b	HOMO (eV)	LUMO (eV) ^c
1	0.34	2.27	-5.14	-2.86
2	0.33	2.36	-5.13	-2.77
3	0.33	2.42	-5.13	-2.71

Half-wave potential ($E_{1/2}$). ^bOptical bandgap. ^c $E_{LUMO} = E_g + E_{HOMO}$.

4. Theoretical Calculation

Computational studies based on time-dependent (TD)-density functional theory (DFT) were performed at the PBE0/6-31G(d,p) level to gain insight into the geometric and electronic properties of compounds **1-3** in their ground state and excited state. The optimized ground state (S_0) structures show the large dihedral angles (θ) between donor and acceptor are close to 90° comparable to that found in the crystal structure of **2**. As a result, the HOMOs and LUMOs are well-separated and are localized on the donor and acceptor moieties, respectively, a typical feature of D-A molecules (**Figure 27**).

To explore the contribution of the T_2 (3LE) state to the RISC process, the SOC matrix elements were calculated using B3LYP functional. The natural transition orbitals (NTO) of compounds **1-3** show that both S_1 and T_1 states originate from donor to acceptor CT transition. Since S_1-T_1 SOC is inefficient due to the CT character of both excited states according to El-Sayed rule,²⁶ the strong SOC between the next upper-lying triplet state (T_2) should be further investigated. For all compounds, the SOC matrix elements between their 3CT and 1CT states were very small ($\langle ^1CT | \hat{H}_{SOC} | ^3CT \rangle = 0.007 \text{ cm}^{-1}$ for PXZBAO and PXZBPO and 0.023 cm^{-1} for PXZBTO, respectively), whereas the values between 3LE and 1CT state were very large ($\langle ^1CT | \hat{H}_{SOC} | ^3LE \rangle = 0.141, 0.125$ and 0.058 cm^{-1} for PXZBAO, PXZBTO and PXZBPO, respectively). Since the strong nonadiabatic vibronic coupling between the 3CT (T_1) and 3LE (T_2) $\langle ^3CT | \hat{H}_{VC} | ^3LE \rangle$, is considered to be particularly stronger than SOC between 3CT and 1CT $\langle ^1CT | \hat{H}_{SOC} | ^3CT \rangle$, it can be inferred that the RISC process can be alternatively accelerated by the strong SOC between T_2 (3LE) and S_1 (1CT) states.

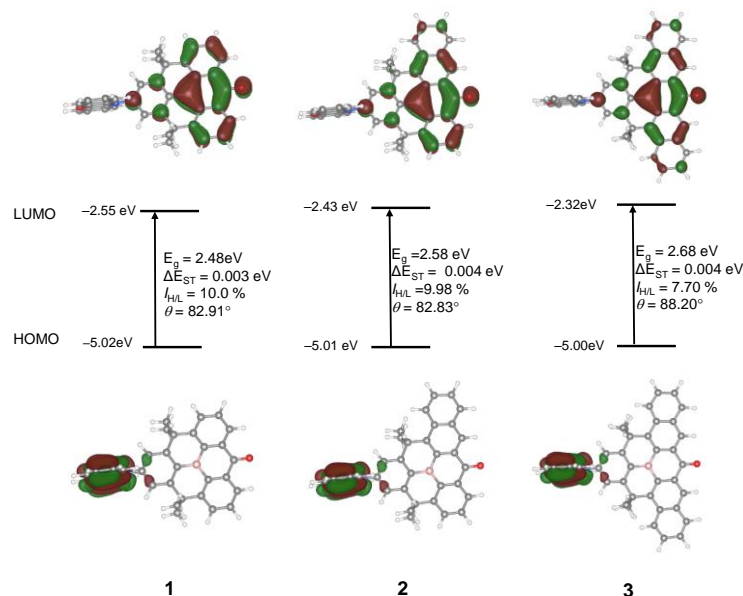


Figure 27. Frontier MOs (HOMO and LUMO) of PXZBAO (1), PXZBTO (2), PXZBPO (3) at their ground state (S_0) geometries obtained by PBE0/6-31G(d,p) calculations. The MO energies, dihedral angles ($\theta = \angle \text{donor} - \angle \text{acceptor}$), HOMO-LUMO gaps (E_g), S_1 - T_1 energy splitting (ΔE_{ST}), and overlap integral extent (I_{HL}) are shown.

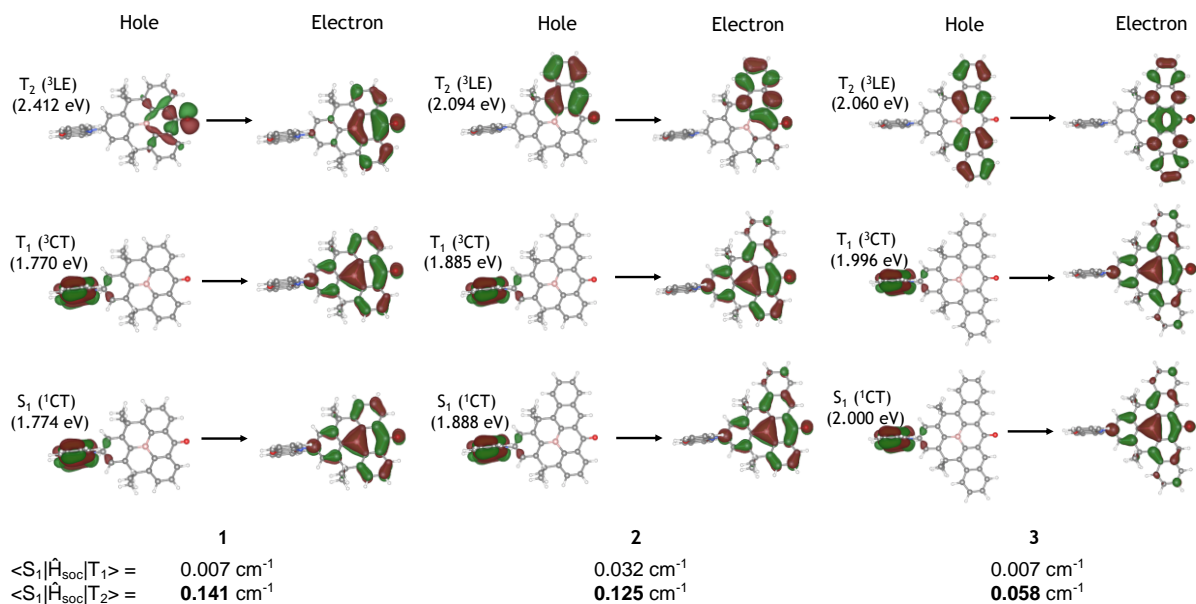


Figure 28. Natural transition orbitals (NTOs) of compounds PXZBAO (1), PXZBTO (2), and PXZBPO (3) for the transitions from the S_0 state to the S_1 , T_1 , and T_2 states obtained using the TDDFT calculations at the PBE0/6-31G(d,p) level of theory. SOC matrix elements are given in the bottom. SOC matrix elements were obtained using B3LYP functional.

5. Electroluminescent Properties

To evaluate the electroluminescent (EL) properties of the proposed emitter (**D1-D3**), TADF-OLED devices were fabricated (**Figure 4a**). The EL characteristics of the three devices are summarized in **Figure 29** and **Table 7**. The emission peak was determined to be 612 nm for **D1**, 584 nm for **D2**, and 566 nm for **D3**, corresponding to the 1931 Commission Internationale de L'Eclairage (CIE) coordinates of (0.591, 0.404) for the red, (0.534, 0.456) for the orange, and (0.469, 0.520) for the yellow. **Figure 4d** display the EQE-luminance characteristics of the devices. The values were 12.8% for **D1**, 15.0% for **D2**, and 17.3% for **D3** which correspond to 23.5 cd A⁻¹ and 17.6 lm W⁻¹ for **D1**, 43.0 cd A⁻¹ and 37.5 lm W⁻¹ for **D2**, and 62.7 cd A⁻¹ and 50.5 lm W⁻¹ for **D3**. The lower device efficiencies of **D1** compared with those of **D2** and **D3** are mainly due to the relatively low PLQY.

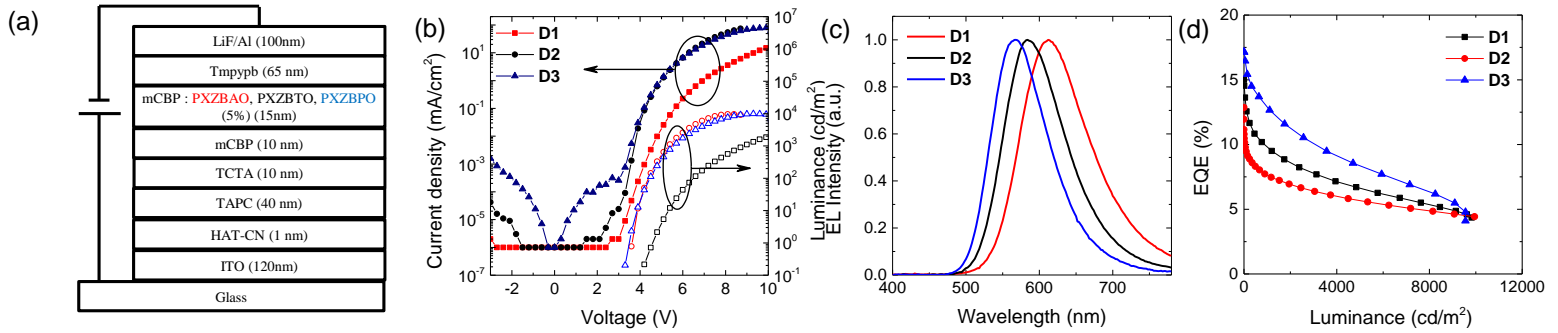


Figure 29. (a) Device Structure of the proposed TADF-OLEDs. (b) Current density-voltage-luminance (J - V - L) characteristics of **D1-D3**. (c) The EL spectra of **D1-D3**. (d) The EQE-luminance of **D1-D3** in the linear scale.

Table 7. Device performances of TADF-OLEDs fabricated with **1–3**.

Device (emitter)	λ_{EL} (nm)	CIE (x, y) ^a	V_{on} (V) ^b	EQE (%) ^c	PE (lm W ⁻¹) ^d	CE (cd A ⁻¹) ^e
D1 (1)	612	(0.591, 0404)	n.d.	12.8	17.6	23.5
D2 (2)	584	(0.534, 0.456)	3.6	15.0	37.5	43.0
D3 (3)	566	(0.469, 0.520)	3.9	17.3	50.5	62.7

^a Color coordinates (CIE 1931) at maximum luminance.

^b Applied voltage at the luminance of 1000 cd m⁻² (**D1**), and 2000 cd m⁻² (**D2-D3**).

^c External quantum efficiency: maximum and value at 1000 cd m⁻² (**D1**), and 2000 cd m⁻² (**D2-D3**).

^d Power efficiency: maximum and value at 1000 cd m⁻² (**D1**), and 2000 cd m⁻² (**D2-D3**).

^e Current efficiency: maximum and value at 1000 cd m⁻² (**D1**), and 2000 cd m⁻² (**D2-D3**)

IV. CONCLUSION

Planarized boron-carbonyl hybrid compounds containing 10*H*-Phenoxazine (PXZ) donor and different acceptors (PXZBAO, PXZBTO, and PXZBPO) were successfully synthesized and characterized through NMR spectroscopy, X-ray crystallography, elemental analysis. All compounds were confirmed to have small singlet-triplet energy splitting ($\Delta E_{ST} < 0.1$ eV), very short-lived delayed fluorescence lifetime ($\tau_d < 2$ μ s), and high k_{RISC} of ca. 10^6 s⁻¹ in oxygen-free toluene solution and mCBP host film. The compounds exhibited emissions in the orange-to-red region ($\lambda_{PL} = 619$ – 574 nm) in toluene solution. In particular, the emission wavelength was blue-shifted with the increase of the number of the benzene rings in the boron acceptors. From the theoretical study, we can imply that the $^3n\pi^*$ of the BCO unit in all compounds lies on the T₂ level and the spin-orbit coupling (SOC) was occurred between the $^3n\pi^*$ (T₂) state and excited singlet (S₁) states leading to a fast RISC. The result of this study gives the insight of the effect of modification of electronic π -conjugation in the BCO acceptors towards its electronic and photophysical properties.

V. REFERENCES

1. Tao, Y.; Yang, C.; Qin, J., Organic host materials for phosphorescent organic light-emitting diodes. *Chem. Soc. Rev.* **2011**, *40*, (5), 2943-70.
2. Helfrich, W.; Schneider, W. G., Recombination radiation in anthracene crystals. *Phys. Rev. Lett.* **1965**, *14* (7), 229-231
3. Tang, C. W.; VanSlyke, S. A., Organic electroluminescent diodes. *Appl. Phys. Lett.* **1987**, *51* (12), 913-915.
4. Yang, Z.; Mao, Z.; Xie, Z.; Zhang, Y.; Liu, S.; Zhao, J.; Xu, J.; Chi, Z.; Aldred, M. P., Recent advances in organic thermally activated delayed fluorescence materials. *Chem. Soc. Rev.* **2017**, *46* (3), 915-1016.
5. Huang, T.; Jiang, W.; Duan, L., Recent progress in solution processable TADF materials for organic light-emitting diodes. *J. Mater. Chem. C.* **2018**, *6*, 5577-5596.
6. Hong, G.; Gan, X.; Leonhardt, C.; Zhang, Z.; Seibert, J.; Busch, J. M.; Bräse, S., A brief history of oleds—emitter development and industry milestones. *Adv. Mater.* **2021**, *33*, 2005630.
7. Im, Y.; Kim, M.; Cho, Y. J.; Seo, J. A.; Yook, K. S.; Lee, J. Y., Molecular design strategy of organic thermally activated delayed fluorescence emitters. *Chem. Mater.* **2017**, *29*, (5), 1946-1963.
8. Lee, H.; Karthik, D.; Lampande, R.; Ryu, J. H.; Kwon, J. H., Recent advancement in boron-based efficient and pure blue thermally activated delayed fluorescence materials for organic light emitting diodes. *Front. Chem.* **2020**, *8*, 373.
9. Wong, M. Y.; Zysman-Colman, E., Purely organic thermally activated delayed fluorescence materials for organic light-emitting diodes. *Adv. Mater.* **2017**, *29*, 1605444.
10. Lee, Y. H.; Park, S.; Oh, J.; Woo, S.-J.; Kumar, A.; Kim, J.-J.; Jung, J.; Yoo, S.; Lee, M. H., High-efficiency sky blue to ultradeep blue thermally activated delayed fluorescent diodes based on ortho-carbazole-appended triarylboron emitters: above 32% external quantum efficiency in blue devices. *Adv. Opt. Mater.* **2018**, *6* (17), 1800385.
11. Ahn, D. H.; Kim, S. W.; Lee, H.; Ko, I. J.; Karthik, D.; Lee, J. Y.; Kwon, J. H., Highly efficient blue thermally activated delayed fluorescence emitters based on symmetrical and rigid oxygen-bridged boron acceptors. *Nat. Photonics.* **2019**, *13*, 540-546.
12. Karthik, D.; Jung, Y. H.; Lee, H.; Hwang, S.; Seo, B. M.; Kim, J. Y.; Han, C.W.; Kwon, J. H., Acceptor-donor-acceptor-type orange-red thermally activated delayed fluorescence materials realizing external quantum efficiency over 30% with low efficiency roll-off. *Adv. Mater.* **2021**, *33*, 2007724.
13. Lee, Y. H.; Shin, Y. S.; Lee, T.; Jung, J.; Lee, J. H.; Lee, M. H., Managing local triplet excited states of boron-based tadf emitters for fast spin-flip process; toward highly efficient

- TADF-OLEDs with low efficiency roll-off. *Chem. Eng. J.* **2021**, *421*, 130224.
14. Olivier, Y.; Yurash, B.; Muccioli, L.; D'Avino, G.; Mikhnenko, O.V.; Sancho-García, J.C.; Adachi, C.; Nguyen, T.; Beljonne, D., Nature of the singlet and triplet excitations mediating thermally activated delayed fluorescence. *Phys. Rev. Mater.* **2017**, *1*, 075602.
 15. Etherington, M.; Gibson, J.; Higginbotham, H.; Penfold, T. J.; Monkman, A. P., Revealing the spin–vibronic coupling mechanism of thermally activated delayed fluorescence. *Nat Commun.* **2016**, *7*, 13680.
 16. Baba, M., Intersystem crossing in the $^1n\pi^*$ and $^1\pi\pi^*$ states. *J. Phys. Chem. A.* **2011**, *115*, (34), 9514-9519.
 17. Wada, Y.; Nakagawa, H.; Matsumoto, S.; Wakisaka, Y.; Kaji, H., Organic light emitters exhibiting very fast reverse intersystem crossing. *Nat. Photonics.* **2020**, *14*, 643-649.
 18. Kim, J. U.; Park, I. S.; Chan, C. Y.; Tanaka, M.; Tsuchiya, Y.; Nakanotani, H.; Adachi, C., Nanosecond-time-scale delayed fluorescence molecule for deep-blue OLEDs with small efficiency rolloff. *Nat Commun.* **2020**, *11*, 1765.
 19. Noda, H.; Nakanotani, H.; Adachi, C., Excited state engineering for efficient reverse intersystem crossing. *Sci. Adv.* **2018**, *4*, eaa06910.
 20. Kushida, T.; Shirai, S.; Ando, N.; Okamoto, T.; Ishii, H.; Matsui, H.; Yamagishi, M.; Uemura, T.; Tsurumi, J.; Watanabe, S.; Takeya, J.; Yamaguchi, S., Boron-stabilized planar neutral π -radicals with well-balanced ambipolar charge-transport properties. *J. Am. Chem. Soc.* **2017**, *139*, (41), 14336-14339.
 21. Link, A.; Fischer, C.; Sparr, C., Direct transformation of esters into arenes with 1,5-bifunctional organomagnesium reagents. *Angew. Chem. Int. Ed.* **2015**, *54*, 12613-12166.
 22. Wood, T. K.; Piers, W. E.; Keay, B. A.; Parvez, M., Synthesis and comparative characterization of 9-boraanthracene, 5-boranaphthacene, and 6-borapentacene stabilized by the H₂IMes carbene. *Chem. Eur. J.* **2010**, *16*, (40) 12199-12206.
 23. Chen, X. L.; Jia, J. H.; Yu, R.; Liao, J. Z.; Yang, M. X.; Lu, C. Z., Combining charge-transfer pathways to achieve unique thermally activated delayed fluorescence emitters for high-performance solution-processed, non-doped blue OLEDs. *Angew Chem Int Ed.* **2017**, *56* (47), 15006-15009.
 24. Meng, G.; Chen, X.; Wang, X.; Wang, N.; Peng, T.; Wang, S., Isomeric Bright Sky-Blue TADF Emitters Based on Bisacridine Decorated DBNA: Impact of Donor Locations on Luminescent and Electroluminescent Properties. *Adv. Opt. Mater.* **2019**, *7* (11).
 25. Schleyer, P. von R.; Manoharan, M.; Wang, Z. X.; Kiran, B.; Jiao, H.; Puchta, R.; van Eikema Hommes, N. J. R., Dissected Nucleus-Independent Chemical Shift Analysis of π -Aromaticity and Antiaromaticity. *Org. Lett.* **2001**, *3* (16), 2465–2468
 26. Lower, S. K.; El-Sayed, M. A., The Triplet state and molecular electronic processes in

organic molecules. *Chem. Rev.* **1966**, *66*, (2), 199-241.